日本磁気学会
ISSN 2432-0250
Journal of the Magnetics Society of Japan
Electronic Journal URL: https://www.jstage.jst.go.jp/browse/msjmag

Vol.43 No.4　2019

Journal

JOURNAL OF THE MAGNETICS SOCIETY OF JAPAN

Vol.43 No.4 2019

日本磁気学会

ISSN 2432-0250

HP: http://www.magnetics.jp/ e-mail: msj@bj.wakwak.com
Electronic Journal: http://www.jstage.jst.go.jp/browse/msjmag

有限要素法解析ソフトウェア COMSOL Multiphysics®

COMSOL MULTIPHYSICS®

マルチフィジックスの進化論

無制限・強連成で実現象に即したシミュレーション事例のご紹介

永久磁石を利用した磁気軸受の解析例

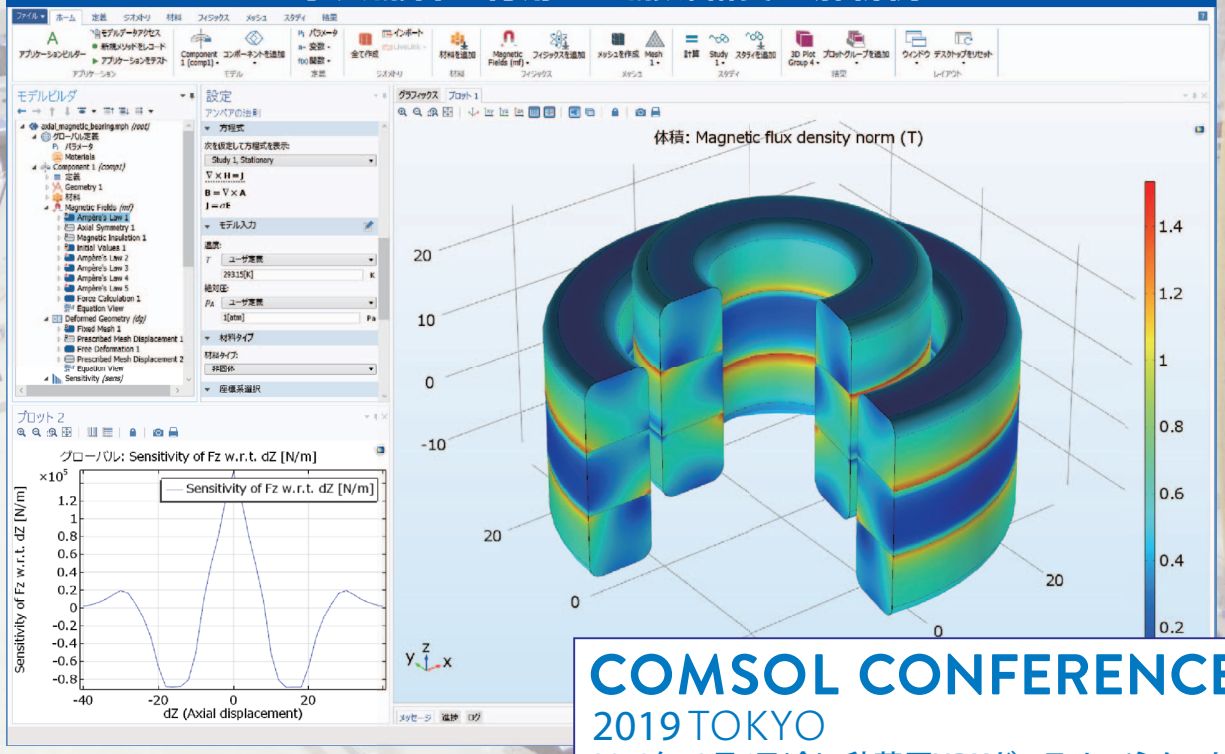

COMSOL CONFERENCE 2019 TOKYO

2019年12月6日(金)：秋葉原UDXギャラリー/ネクスト

https://kesco.co.jp/conference/

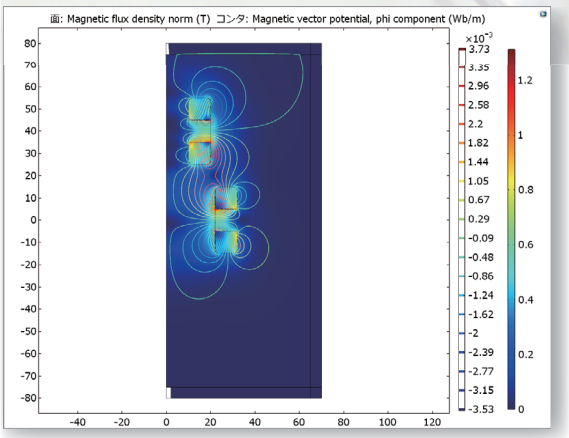

AC/DC モジュールの適用例

- AC/DC 電流分布、電場分布
- バイオヒーティング
- コイルとソレノイド
- SPICE 回路とフィールドシミュレーション
- 接触抵抗
- 電磁両立性 (EMC) および電磁妨害 (EMI)
- 電磁力およびトルク
- 電磁力シールド
- 電気機械の変形
- ホール効果を利用したセンサ
- インシュレータ、コンデンサ、誘電体
- モータ、ジェネレータ、および他の電気機械
- 非線形材料
- 寄生容量とインダクタンス
- 永久磁石と電磁石
- 多孔質材料
- 抵抗および誘導加熱
- センサ
- 超伝導体
- 変圧器とインダクタ

永久磁石を使用した磁気軸受の解析例

永久磁石を使用した軸受はターボ機械、ポンプ、モータ、発電機やフライホイール式エネルギー貯蔵システムなど、様々な分野で使用されています。非接触かつ潤滑不要で保守整備を大幅に省略できる点は、従来の機械式ベアリングと比べて重要なメリットです。
この例では、軸方向の永久磁石軸受の磁気力と剛性などの設計パラメータを計算する方法を示しています。

※AC/DCモジュールはCOMSOL Multiphysics®と併用するアドオン製品です。

COMSOL Multiphysics® なら、今まで不可能だった 3 種以上のマルチフィジックス解析を強連成で実現できます。30 日間全機能無料トライアル、無料の導入セミナー、1000種を超える世界の様々な事例をご提供いたします。詳しくは、下記の弊社営業部までお問い合せください。

COMSOL

http://www.comsol.jp

KESCO KEISOKU ENGINEERING SYSTEM
計測エンジニアリングシステム株式会社
https://kesco.co.jp/service/comsol/
Tel : 03-5282-7040 ・ Fax : 03-5282-0808

INDEX

世界初！
高温超電導型VSM

新製品

世界初*、高温超電導マグネットをVSMに採用することで
測定速度 当社従来機1/20を実現。
0.5mm cube磁石のBr, HcJ高精度測定が可能と
なりました。
*2014年7月 東英工業調べ

測定結果例

高温超電導VSMによるNdFeB(sint.) 0.5mm cube BHカーブ

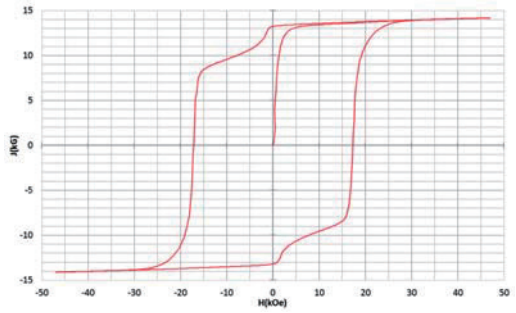

磁化測定レンジ：0.2emu
Br = 13.2kG　　HcJ = 17.2kOe

高温超電導VSMによるNdFeB(sint.) 1mm cube BHカーブ

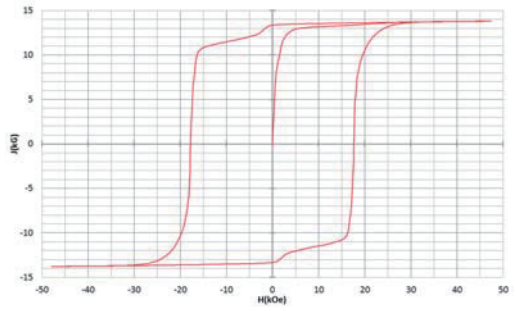

磁化測定レンジ：2emu
Br = 13.3kG　　HcJ = 17.7kOe

高温超電導VSMによるNdFeB(sint.) 4mm cube BHカーブ

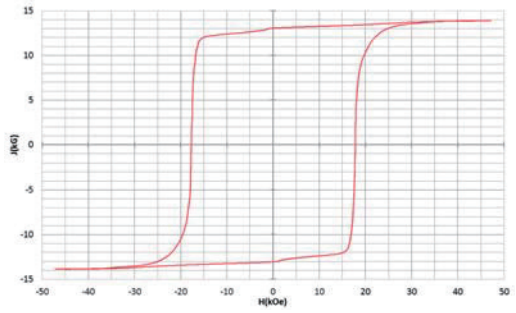

磁化測定レンジ：100emu
Br = 13.1kG　　HcJ = 17.8kOe

高速測定を実現

高温超電導マグネット採用により、高速測定を実現しました。Hmax= 5Tesla, Full Loop 測定が2分で可能です。
（当社従来機：Full Loop測定　40分）

小試料のBr,HcJ高精度測定

0.5mm cube 磁石のBr,HcJ高精度測定ができ、表面改質領域を切り出しBr,HcJの強度分布等、微小変化量の比較測定が可能です。
また、試料の加工劣化の比較測定が可能です。

試料温度可変測定

−50℃～+200℃温度可変UNIT（オプション）

磁界発生部の小型化

マグネットシステム部寸法：0.8m×0.3m×0.3m

TOEI 東英工業株式会社
http://www.toeikogyo.co.jp
〒194-0035 東京都町田市忠生1-8-13
TEL：042-791-1211 FAX：042-792-0490
E-mail : sales@toeikogyo.co.jp

Journal of the Magnetics Society of Japan
Vol. 43, No. 4

Electronic Journal URL: https://www.jstage.jst.go.jp/browse/msjmag

CONTENTS

J. Magn. Soc. Jpn., **43**, 70-78 (2019)

<Paper>

Impact of Curie Temperature Variation on Bit Error Rate in Heat-Assisted Magnetic Recording

T. Kobayashi, Y. Nakatani*, and Y. Fujiwara

Graduate School of Engineering, Mie Univ., *1577 Kurimamachiya-cho, Tsu 514-8507, Japan*

*Graduate School of Informatics and Engineering, Univ. of Electro-Communications, *1-5-1 Chofugaoka, Chofu 182-8585, Japan*

The Curie temperature T_c variation problem in heat-assisted magnetic recording is discussed. We describe the physical implication of the T_c variation problem, and provide ways of improving the writing property by employing our simplified model calculation. The bit error rates for mean Curie temperatures of 600 and 700 K are examined. The T_c variation increases both write-error (WE) and erasure-after-write (EAW). The main related calculation parameters are the grain column number in one bit and the thermal gradient for the down-track direction. Increasing the grain column number is effective in reducing WE and EAW caused by the T_c variation. Furthermore, increasing the thermal gradient is necessary since EAW is high. Although a higher writing field of 12 to 14 kOe is necessary, a bit error rate less than 10^{-3} can be achieved for recording densities of 4 or 2 Tbpsi under the conditions used in this study even though the standard deviation of the Curie temperature is 4 %.

Key words: heat-assisted magnetic recording, field sensitivity, Curie temperature, variation

1. Introduction

Heat-assisted magnetic recording (HAMR) is a promising candidate as a next generation magnetic recording method that can operate beyond the trilemma limit[1].

We have already proposed a new HAMR model calculation[2)~4)]. We have also shown in our improved model calculation that the signal-to-noise ratio derived by the conventionally used micromagnetic calculation can be explained using the temperature dependences of the grain magnetization reversal probability and the attempt period, whose inverse is the attempt frequency[5]. A feature of our model calculation is that it is easy to grasp the physical implication of the HAMR writing process and the calculation time is short.

Since HAMR is a writing method in which the medium is heated to reduce coercivity at the time of writing, the coercivity of the medium can be reduced by any amount. However, micromagnetic simulation has shown that a relatively high writing field is necessary[6].

The actual HAMR system is very complicated, and various problems are intertwined. Therefore, we have separated problems in a simplified model using our model calculation. We have divided the topic of increasing writing field sensitivity into four problems using the bit error rate calculated with our model for HAMR, and we have discussed the calculation parameters related to the problems[7]. The four problems are write-error, erasure-after-write[6], a statistical problem[7], and the damping constant[3].

It has been reported that variation in the Curie temperature T_c is a serious problem in HAMR[8]. In this study, we discuss a fifth problem, namely the T_c variation problem, and we provide some ways of improving the writing property employing our model calculation.

2. Calculation Method

2.1 Calculation conditions

The areas S of one bit are 161 and 323 nm^2 for recording densities of 4 and 2 Tbpsi, respectively. The medium was assumed to be bit patterned media (BPM).

The writing field switching timings for an ordinary granular medium and this BPM model are shown in Figs. 1 (a) and (b), respectively. H_w and $\tau_{min} = D_{BP}/v$ are the writing field and the time available for writing each bit, respectively, where D_{BP} and v are the bit pitch and the linear velocity, respectively. There is a fluctuation of switching timing Δt in an ordinary granular medium as shown in Fig. 1 (a). However, we assume $\Delta t = 0$, and when the time $t = 0$, the writing grain temperature T becomes the mean Curie temperature T_{cm} as shown in Fig. 1 (b) for our discussion of the intrinsic phenomenon. The problem of Δt is a future subject. The H_w direction is upward between $t = 0$ and τ_{min}, and downward when $t < 0$ and $t > \tau_{min}$.

It was assumed that the spatially uniform writing field moves to the down-track direction successively, the direction was perpendicular to the medium plane, and the rise time was zero. Neither the demagnetizing nor the magnetostatic fields were considered during writing since they are negligibly small.

The grain arrangements for an ordinary granular medium and this BPM model are also shown in Figs. 1 (c) and (d), respectively, for an $m \times n = 4 \times 1$ grain arrangement where m and n are the grain numbers in one bit for the cross-track and down-track directions, respectively. T_{cij} and D_{ij} are the Curie temperature and the grain size, respectively. There is also a fluctuation of position $\Delta x < (D_m + \Delta)/2$ in an ordinary granular medium as shown in Fig. 1 (c) where D_m and Δ are the mean grain size and the non-magnetic

spacing, respectively. However, we assume $\Delta x = 0$ as shown in Fig. 1 (d) in this BPM model, and the problem of Δx is also a future subject. The thermal gradient $\partial T/\partial y$ for the cross-track direction was assumed to be 0 K/nm since complex situations disturb our intrinsic discussion. Although the problem of $\partial T/\partial y$ is also a future subject, $\partial T/\partial y \neq 0$ will affect the results.

The mean grain size D_m was determined by

$$D_m = \sqrt{\frac{S}{mn}} - \Delta \qquad (1)$$

where Δ = 1 nm was assumed. The track and bit pitches were $D_{TP} = m(D_m + \Delta)$ and $D_{BP} = n(D_m + \Delta)$, respectively, and then $S = D_{TP} \cdot D_{BP}$.

The calculation conditions are summarized in Table 1, and the calculation parameters were the recording density, the grain number per bit mn, the mean Curie temperature T_{cm}, the standard deviations of the Curie temperature σ_{Tc}/T_{cm}, the Gilbert damping constant α, the anisotropy constant ratio K_u/K_{bulk}, the linear velocity v, and the thermal gradient $\partial T/\partial x$. $\partial T/\partial x$ was assumed to be constant regardless of the position, and the heat distribution moves to the down-track direction successively. The standard deviation of the grain size σ_D/D_m and the grain height h were 10 % and 8 nm, respectively, and so the grain volume V_m for D_m was $D_m \times D_m \times h$.

The medium was characterized by (1) T_{cm}, (2) α, and (3) K_u/K_{bulk}, which is the intrinsic ratio of the medium anisotropy constant K_u to bulk FePt K_u[9].

(1) If T_{cm} is low, a larger K_u/K_{bulk} is necessary[10]. Therefore, we chose T_{cm} values of 600 and 700 K. The standard deviations of the Curie temperature σ_{Tc}/T_{cm} were assumed to be 0, 2, and 4 %.

(2) The α value of FePt just below the Curie temperature T_c is unknown. Therefore, we calculated the bit error rate using α = 0.1 and 0.01.

(3) The K_u/K_{bulk} value must be larger than the value required for 10 years of archiving.

Figure 2 shows the minimum K_u/K_{bulk} value for 10 years of archiving as a function of the mean grain size D_m. The inserted scales indicate the grain number per bit mn corresponding to D_m for recording densities of 4 and 2 Tbpsi. The minimum $K_u(300\ \mathrm{K})$ value was roughly estimated using

$$\frac{K_u(300\ \mathrm{K})V_m}{kT} > 60 \qquad (2)$$

where k and T = 300 K are the Boltzmann constant and temperature, respectively. And then, the minimum K_u/K_{bulk} value was obtained using the relationship between $K_u(300\ \mathrm{K})$ and T_c for various K_u/K_{bulk} values[7].

It is also confirmed from Fig. 2 that if T_{cm} is low, a larger K_u/K_{bulk} is necessary[10]. Experimentally obtained results, namely those for FeNiPt[11] and FePtRu[12] films, are at most between K_u/K_{bulk} = 0.4 and 0.6[7].

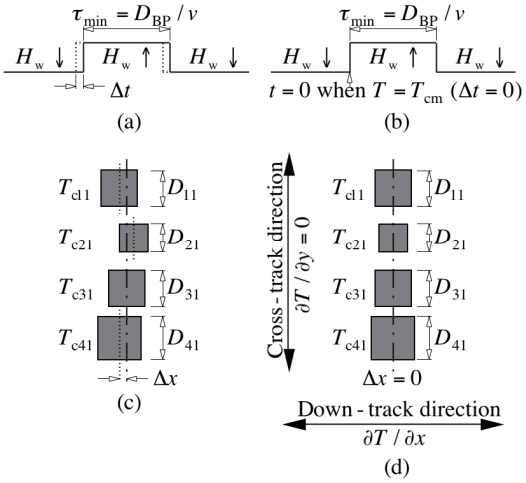

Fig. 1 (a), (b) Writing field switching timing, and (c), (d) grain arrangement for (a), (c) an ordinary granular medium and (b), (d) this BPM model.

Table 1 Calculation conditions.

Recording density (Tbpsi)	2, 4
Grain number per bit mn (1/bit)	4, 9, 16
Standard deviation of grain size σ_D/D_m (%)	10
Grain height h (nm)	8
Mean Curie temperature T_{cm} (K)	600, 700
Standard deviation of Curie temp. σ_{Tc}/T_{cm} (%)	0, 2, 4
Gilbert damping constant α	0.1, 0.01
Linear velocity v (m/s)	5, 10
Thermal gradient $\partial T/\partial x$ (K/nm)	15, 20

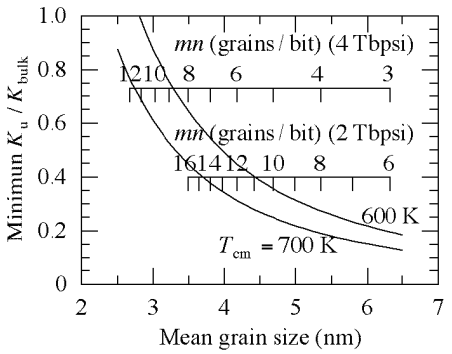

Fig. 2 Minimum anisotropy constant ratio K_u/K_{bulk} necessary for 10 years of archiving as a function of mean grain size.

2.2 Bit error rate calculation

The magnetization direction of the grains was calculated using the magnetization reversal probability for every attempt time in our model calculation[2)~5),7)].

The initial magnetization direction, namely upward or downward, is randomly decided. The switching probability P_{-} for each attempt where the magnetization M_s and the writing field H_w change

from antiparallel to parallel is expressed as

$$P_{-} = \exp\left(-K_{\beta-}\right). \tag{3}$$

On the other hand,

$$P_{+} = \exp\left(-K_{\beta+}\right) \tag{4}$$

is the probability for each attempt where M_s and H_w change from parallel to antiparallel. In these equations,

$$K_{\beta-}(T, H_w) = \frac{K_u(T)V}{kT}\left(1-\frac{H_w}{H_k(T)}\right)^2 \quad \left(H_k(T) \geq H_w\right),$$

$$K_{\beta-}(T, H_w) = 0 \quad \left(H_k(T) < H_w\right), \tag{5}$$

and

$$K_{\beta+}(T, H_w) = \frac{K_u(T)V}{kT}\left(1+\frac{H_w}{H_k(T)}\right)^2, \tag{6}$$

where K_u, V, k, T, and $H_k = 2K_u/M_s$ are the anisotropy constant, the grain volume, the Boltzmann constant, the writing grain temperature, and the anisotropy field, respectively.

The temperature dependence of M_s was determined by employing a mean field analysis[13], and that of K_u was assumed to be proportional to M_s^2[11]. The Curie temperature T_c was adjusted by the Cu simple dilution of $(Fe_{0.5}Pt_{0.5})_{1-z}Cu_z$. $M_s(T_c, T)$ is a function of T_c and T, and $M_s(T_c = 770\ \mathrm{K}, T = 300\ \mathrm{K})$ = 1000 emu/cm^3 was assumed for FePt (Cu composition z = 0). $K_u(T_c, K_u/K_{bulk}, T)$ is a function of T_c, the anisotropy constant ratio K_u/K_{bulk}, and T. $K_u(T_c = 770\ \mathrm{K}, K_u/K_{bulk} = 1, T = 300\ \mathrm{K})$ = 70 Merg/cm^3 was assumed for FePt (z = 0). We used $M_s(T_c, T)$ and $K_u(T_c, K_u/K_{bulk}, T)$ for T_{cm} = 600 and 700 K in this paper.

On the other hand, the attempt time t_k, whose interval is the mean of the attempt period τ_{AP}, is determined in the following[5]. The inverse of the attempt period is the attempt frequency $f_0 = 1/\tau_{AP}$. Since there was a very good linear relationship between f_0 and T, we used

$$f_0(T) = \frac{2a\alpha}{1+\alpha^2}\sqrt{\frac{V}{V_0}}\frac{K_u/K_{bulk}}{0.4}(T_c - T) \tag{7}$$

where a = 4.67 and 5.0 (nsK)$^{-1}$ for T_{cm} = 600 and 700 K, respectively, and V_0 = 193 nm^3. The f_0 value becomes zero at $T = T_c$ as shown in Eq. (7).

We defined the initial time t_{ini1} at $T = T_{th} = T_c - 1\ \mathrm{K}$, which is close to T_c, using

$$t_{ini1} = \frac{T_c - T_{th}}{v(\partial T/\partial x)} \tag{8}$$

since $\tau_{AP} = 1/f_0$ diverges to infinity at $T = T_c$. The next initial time t_{ini2} was calculated using the mean attempt period τ_{APm} from t_{ini1} to t_{ini2} expressed by

$$t_{ini2} - t_{ini1} = \tau_{APm} = \frac{1}{t_{ini2} - t_{ini1}}\int_{t_{ini1}}^{t_{ini2}} \tau_{AP}(t)dt\ . \tag{9}$$

We assumed that the first attempt time t_1 is randomly decided between t_{ini1} and t_{ini2}. And the attempt time t_{k+1} $(k \geq 1)$ is determined with the following recurrence formula:

$$t_{k+1} - t_k = \tau_{APm} = \frac{1}{t_{k+1} - t_k}\int_{t_k}^{t_{k+1}} \tau_{AP}(t)dt\ . \tag{10}$$

Errors occur in some grains of a bit. We assume that if the surface magnetic charge of the grains where the magnetization turns in the recording direction $\sum M_{ij}(T_c, 300\ \mathrm{K})D_{ij}^2$ is more than 50 % of the total surface magnetic charge in one bit, the bit is error free. Namely, if

$$\frac{\sum_{i,j} M_{ij}(T_c, 300\ \mathrm{K})D_{ij}^2}{mn \cdot M_s(T_{cm}, 300\ \mathrm{K})D_m^2} > 0.5, \tag{11}$$

the bit is error free. The number of calculation bits is 10^5. The criterion determining whether or not recording is possible was assumed to be a bit error rate (bER) of 10^{-3}. Increasing the writing field sensitivity means lowering the writing field at which the bER value is 10^{-3}. The bER in this study is useful only as a comparison.

The calculation procedure is described below. First, the medium was characterized by T_{cm}, α, and K_u/K_{bulk}. The grain temperature fell with time from T_c according to the linear velocity v and the thermal gradient $\partial T/\partial x$ for the down-track direction. The attempt times were calculated. The magnetic property and then $P_{\pm}$ were calculated by undertaking a mean field analysis for every attempt time. The magnetization direction was determined by the Monte Carlo method for every attempt time. Then the bER was obtained.

3. Calculation Results

We have divided the topic of increasing the writing field sensitivity into four problems for heat-assisted magnetic recording, and we have discussed the calculation parameters related to the problems[7] as follows.

(1) Write-error problem

Reducing the anisotropy constant ratio K_u/K_{bulk} and/or the linear velocity v is effective in reducing write-error (WE), namely, in increasing the writing field sensitivity.

(2) Erasure-after-write problem

Erasure-after-write (EAW) must be sufficiently low in a low writing field region. Increasing K_u/K_{bulk}, the thermal gradient $\partial T/\partial x$ for the down-track direction, and/or the grain column number in one bit n is effective in reducing EAW.

(3) Statistical problem

Increasing the grain number per bit mn under a constant mean grain size is effective in increasing the

writing field sensitivity for a statistical reason. However, increasing mn under a constant recording density is ineffective when there is no Curie temperature variation. Nevertheless, there is a statistical effect since the recording time window decreases and the attempt period increases.

(4) Damping constant problem

When the Gilbert damping constant α is small, writing is difficult and a high writing field is necessary since the attempt period is long. Reducing v is effective in increasing the writing field sensitivity since WE is dominant for a small α.

In this study, we discuss a fifth problem, namely:

(5) Curie temperature variation problem

The main related parameters are n and $\partial T/\partial x$.

3.1 α = 0.1, T_{cm} = 700 K, and $\partial T/\partial x$ = 15 K/nm

First, we deal with the damping constant α = 0.1, the mean Curie temperature T_{cm} = 700 K, and the thermal gradient $\partial T/\partial x$ = 15 K/nm. As shown in a previous paper[7], when α = 0.1, T_{cm} = 700 K, and the standard deviation of the Curie temperature σ_{Tc}/T_{cm} = 0 %, a 4 Tbpsi recording (4×1 grain arrangement) can be achieved as shown in Fig. 3, which shows the bit error rate (bER) dependence on writing field H_w. An anisotropy constant ratio K_u/K_{bulk} of about 0.35 is the best condition[7] under a linear velocity v of 10 m/s and a thermal gradient $\partial T/\partial x$ of 15 K/nm even though the minimum K_u/K_{bulk} value for 10 years of archiving is 0.19 as shown in Fig. 2. If there is a Curie temperature T_c variation, the signal-to-noise ratio will be degraded[8], and then the bER will increase as shown in Fig. 3. The decrease and increase in bER as H_w increases are caused by a reduction in the write-error (WE) and an increase in erasure-after-write (EAW)[6], respectively. Therefore, the T_c variation increases both WE and EAW.

This is explained using Fig. 4, which shows the time dependence of the grain magnetization reversal probabilities P_- for grains with T_c of $T_{cm}+\sigma_{Tc}$, T_{cm}, and $T_{cm}-\sigma_{Tc}$. The filled circles indicate the attempt times t_k when $t_1 = t_{ini1}$ and $t_2 = t_{ini2}$. In this paper, figures of P_- with time are shown in the same format.

The time t = 0 is the onset of the writing time, which corresponds to the 1st column grain temperature becoming T_{cm}. The attempt frequency f_0 is low just below T_c as shown in Eq. (7), and then the attempt period $\tau_{AP} = 1/f_0$ is long just after t = 0 for a grain with $T_c = T_{cm}$. The temperature decreases with time, and the mean attempt period τ_{APm}, which is the interval between the attempt times, decreases accordingly. The time $t = \tau_{min}$ is the end of the writing time, which corresponds to the time available for writing each bit and $\tau_{min} = D_{BP}/v$ as shown in Fig. 1.

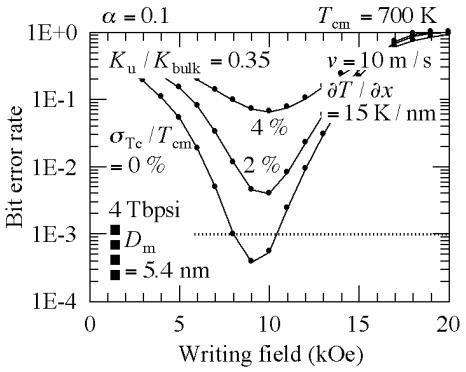

Fig. 3 Dependence of bit error rate on writing field for various standard deviations of Curie temperature σ_{Tc}/T_{cm} (α = 0.1, T_{cm} = 700 K, 4×1 grain arrangement).

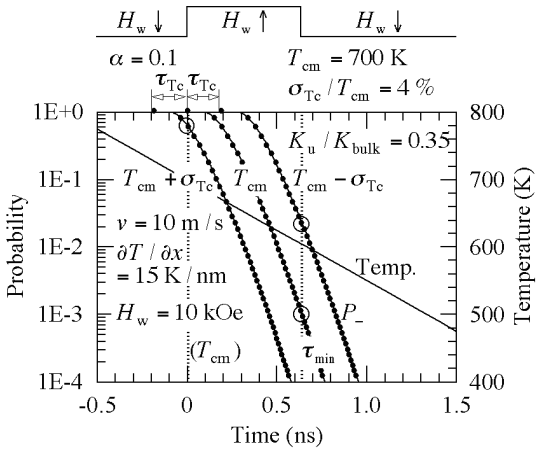

Fig. 4 Time dependence of grain magnetization reversal probabilities P_- and temperature for grains with Curie temperatures of $T_{cm}+\sigma_{Tc}$, T_{cm}, and $T_{cm}-\sigma_{Tc}$.

WE means that the magnetization does not switch to the recording direction, and WE occurs during writing ($0 \le t \le \tau_{min}$). If there is a T_c variation, WE increases from grains with a higher T_c, for example, $T_c = T_{cm}+\sigma_{Tc}$ in Fig. 4. We introduce a new parameter, namely a Curie temperature variation window τ_{Tc}:

$$\tau_{Tc} = \frac{\sigma_{Tc}}{v(\partial T/\partial x)}. \qquad (12)$$

The writing time is advanced for higher T_c grains, for example, by τ_{Tc} for a grain with $T_c = T_{cm}+\sigma_{Tc}$. Even at a time before zero, the grain temperature is lower than T_c, and then the grain is magnetized in the downward direction, namely opposite to the recording direction. At time zero, the direction of the writing field changes. The P_- value for a grain with $T_c = T_{cm}+\sigma_{Tc}$ at t = 0 designated by the open circle in Fig. 4 is low. Therefore, the probability with which the magnetization reverses to the recording direction is low. Then, WE increases.

On the other hand, EAW is grain magnetization reversal in the opposite direction to the recording

direction caused by changing the H_w direction at the end of the writing time τ_{min}, and EAW occurs after writing ($t > \tau_{min}$). If there is a T_c variation, EAW increases from grains with a lower T_c, for example, $T_c = T_{cm} - \sigma_{Tc}$ in Fig. 4. The writing time is delayed for lower T_c grains, for example, by τ_{Tc} for a grain with $T_c = T_{cm} - \sigma_{Tc}$. The P_- value at τ_{min} is important for EAW. The P_- value for a grain with $T_c = T_{cm} - \sigma_{Tc}$ at τ_{min} designated by the open circle in Fig. 4 is high. Therefore, the probability with which the magnetization reverses to the direction opposite to that of recording is high. Then, EAW increases.

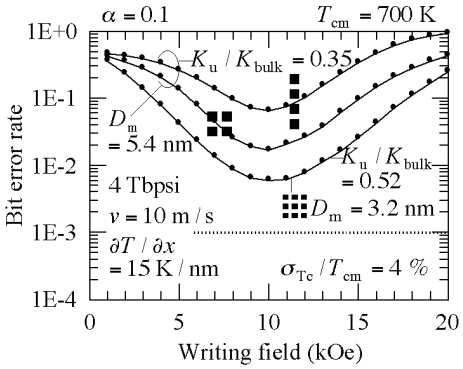

Fig. 5 Dependence of bit error rate on writing field for 4×1, 2×2, and 3×3 grain arrangements (α = 0.1, T_{cm} = 700 K, σ_{Tc}/T_{cm} = 4 %).

Figure 5 shows the bER dependence on H_w for 4×1, 2×2, and 3×3 grain arrangements where σ_{Tc}/T_{cm} is 4 %. A comparison of the bER for $m\times n = 4\times1$ and that for a 2×2 grain arrangement where the grain numbers per bit mn, the K_u/K_{bulk} values, and the mean grain sizes D_m are the same for avoiding these problems, reveals that the bER for the latter is lower than that for the former in all calculated H_w ranges. In other words, both WE and EAW decrease. This is also explained using Fig. 6 in which the time dependences of P_- for (a) the 1st and (b) the 2nd columns of a 2×2 grain arrangement are shown. The P_- values in Fig. 4 and Fig. 6 (a) are identical. However, the τ_{min} value in Fig. 6 is twice that in Fig. 4. The P_- value at τ_{min} in Fig. 6 (a) is sufficiently low even for a grain with $T_c = T_{cm1} - \sigma_{Tc}$. Accordingly, EAW for the 1st column of the 2×2 grain arrangement decreases. On the other hand, the P_- values in Fig. 4 and Fig. 6 (b) are also identical except for time, and the writing time in Fig. 6 (b) is delayed by a time corresponding to the grain pitch $D_m + \Delta$. Consequently, the P_- values at τ_{min} in Fig. 4 and Fig. 6 (b) are the same, and EAW for the 2nd column of the 2×2 grain arrangement does not change. Comprehensively increasing the grain column number n is effective in reducing EAW.

Increasing n is also effective in reducing WE. The H_w switching timings at t = 0 in Fig. 4 and Fig. 6 (a) are identical. Hence, WE for the 1st column of the 2×2 grain arrangement does not change. On the other hand, the writing time for the 2nd column of the 2×2 grain arrangement is delayed by a time corresponding to a grain pitch $D_m + \Delta$ as shown in Fig. 6 (b). The H_w direction is the recording direction even at a time that corresponds to the grain temperature with $T_c = T_{cm2} + \sigma_{Tc}$ becoming T_c. Therefore, WE for the 2nd column of the 2×2 grain arrangement decreases.

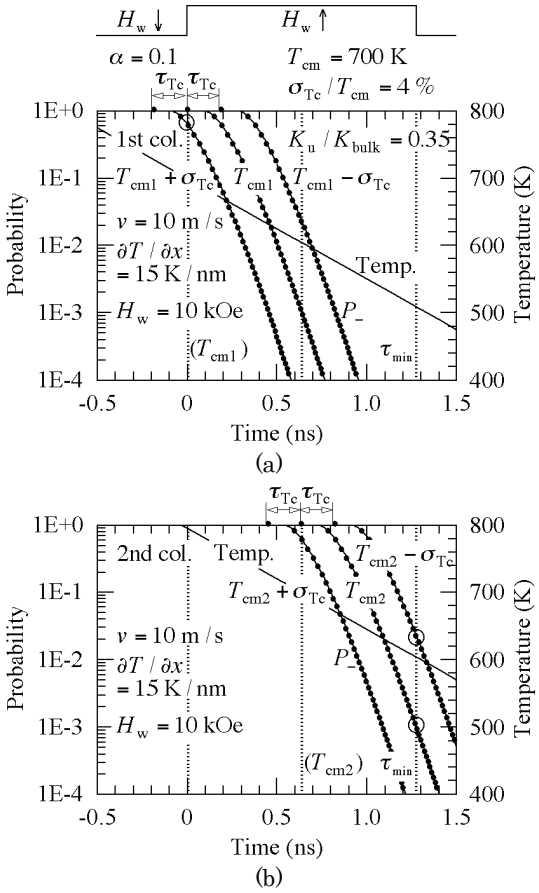

Fig. 6 Time dependence of grain magnetization reversal probabilities P_- and temperature for (a) 1st and (b) 2nd columns of a 2×2 grain arrangement.

Next, we make a comparison between bER for the 2×2 grain arrangement and that for the 3×3 grain arrangement in Fig. 5. It was assumed that σ_{Tc} does not increase even if D_m is reduced. When the 2×2 grain arrangement (the grain number per bit mn = 4), D_m = 5.4 nm, and K_u/K_{bulk} = 0.35 is necessary for a low bER. On the other hand, when the 3×3 grain arrangement (mn = 9), D_m = 3.2 nm, and then K_u/K_{bulk} = 0.52 is necessary for 10 years of archiving.

Reducing D_m, and then increasing n is effective in reducing both WE and EAW as shown in Fig. 5. This is also explained using Fig. 7, which shows the time dependences of P_- for (a) the 1st, (b) the 2nd, and (c) the 3rd columns of the 3×3 grain arrangement. The rate at which P_- decreases with time becomes slow according to Eq. (5), in which K_u, V, and

$H_k = 2K_u / M_s$, namely K_u / K_{bulk} and D_m have different values. Furthermore, the recording time window[6] τ_{RW} becomes short where τ_{RW} is the time for $P_- = 1$, namely $H_k < H_w$ according to Eq. (5). And the attempt period $\tau_{AP} = 1/f_0$ for 3×3 is somewhat longer than that for the 2×2 grain arrangement according to Eq. (7) since $D_m \cdot K_u / K_{bulk}$ for 3×3 is somewhat smaller than that for the 2×2 grain arrangement. Although various factors are involved, the EAW reduction is roughly explained by the fact that the P_- value at τ_{min} in Fig. 7 (b) is smaller than that in Fig. 6 (b). The WE reduction is explained as follows.

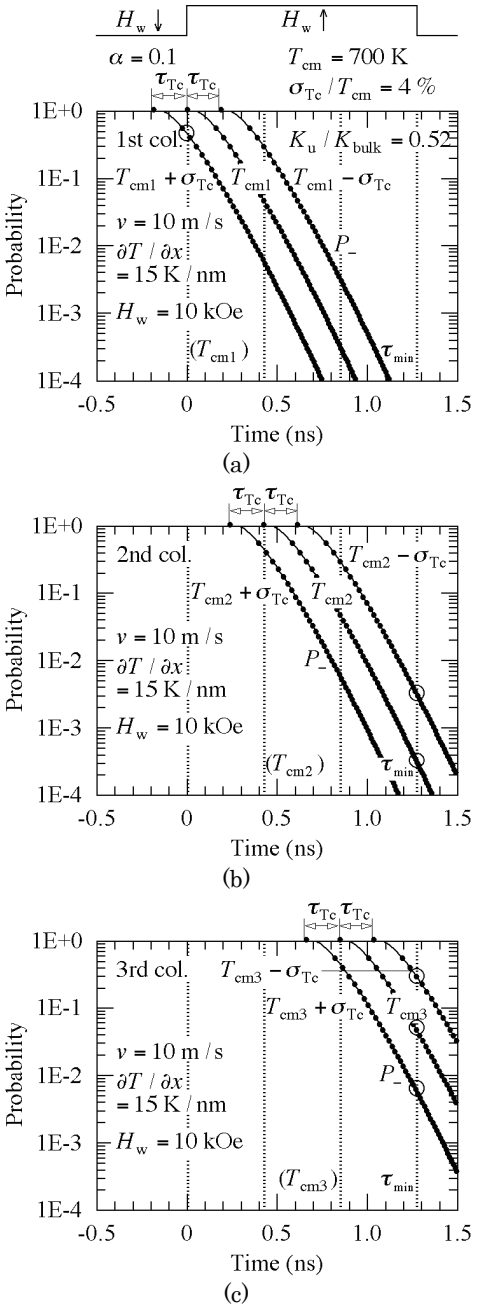

Fig. 7 Time dependence of grain magnetization reversal probabilities P_- for (a) 1st, (b) 2nd, and (c) 3rd columns of the 3×3 grain arrangement.

The H_w direction is the recording direction when the temperature of the 2nd and the 3rd column grains becomes T_c as shown in Figs. 7 (b) and (c), respectively.

3.2 α = 0.1, T_{cm} = 700 K, and $\partial T/\partial x$ = 20 K/nm

A bER less than 10^{-3} cannot be achieved as shown in Fig. 5 since EAW is high. Therefore, we calculate the bER using the thermal gradient $\partial T / \partial x$ = 20 K/nm instead of 15 K/nm for the suppression of EAW. The bER calculation results are shown in Fig. 8. A bER less than 10^{-3} can be achieved for the 3×3 grain arrangement and $\partial T / \partial x$ = 20 K/nm as shown in Fig. 8 (b).

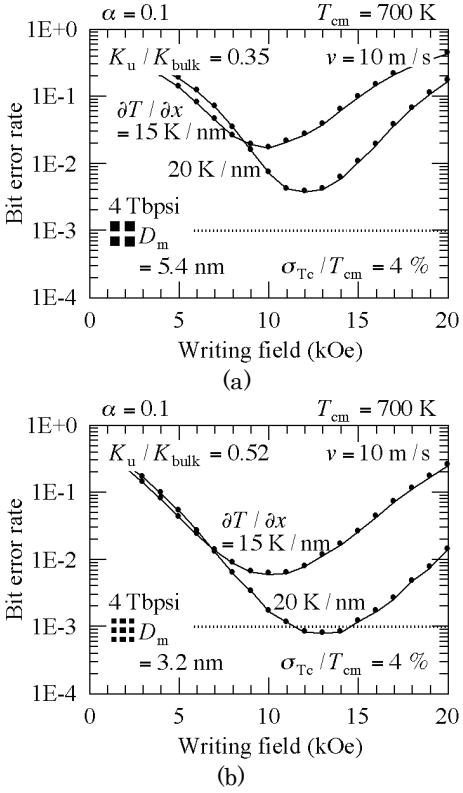

Fig. 8 Dependence of bit error rate on writing field for thermal gradients $\partial T / \partial x$ = 15 and 20 K/nm (α = 0.1, T_{cm} = 700 K, (a) 2×2 and (b) 3×3 grain arrangements).

Figure 9 shows the time dependence of P_- for the respective columns. When $\partial T / \partial x$ increases, the Curie temperature variation window τ_{Tc} will be reduced according to Eq. (12). τ_{Tc} is the time during which grain with $T_c = T_{cm1} + \sigma_{Tc}$ is exposed to H_w opposite to the recording direction as shown Fig. 9 (a). Therefore, the reduction of τ_{Tc} is advantageous for the suppression of WE caused by the T_c variation. On the other hand, as $\partial T / \partial x$ increases, the writing field sensitivity becomes somewhat worse[7] since the rate at which P_- decreases with time becomes steep, and the attempt number is somewhat reduced when P_- is high

as shown in Fig. 9. Comprehensively increasing $\partial T/\partial x$ is not effective in reducing WE as shown in Fig. 8.

As shown in a previous paper[7] and as seen by comparing Fig. 7 and Fig. 9, increasing $\partial T/\partial x$ is effective in reducing EAW since the P_- values at τ_{min} become low. The resultant bER is shown in Fig. 8, and a bER less than 10^{-3} can be achieved. However, a higher writing field is necessary if there is a T_c variation.

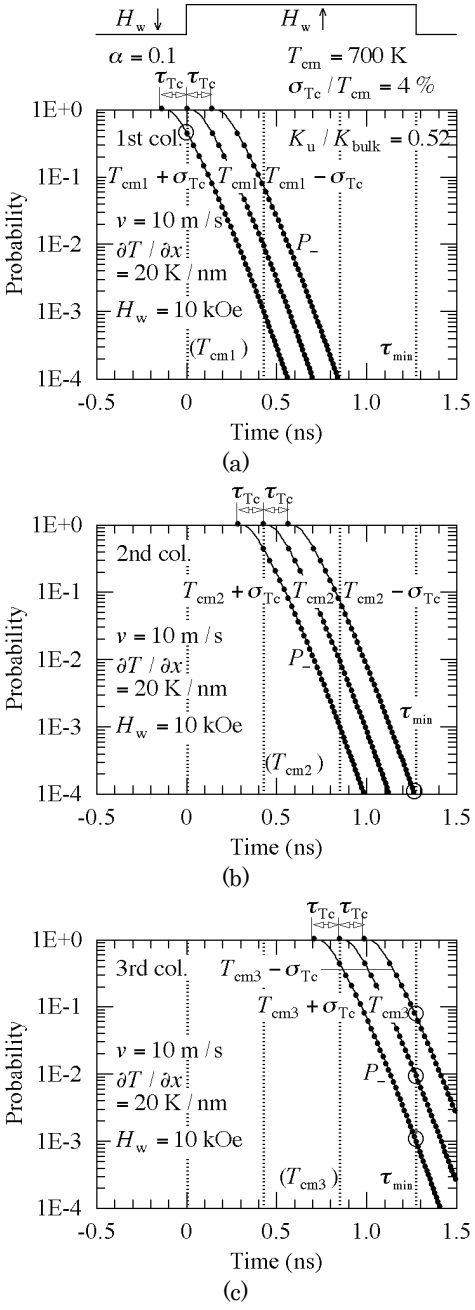

Fig. 9 Time dependence of grain magnetization reversal probabilities P_- for (a) 1st, (b) 2nd, and (c) 3rd columns of the 3×3 grain arrangement ($\partial T/\partial x$ = 20 K/nm).

3.3 α = 0.1 and T_{cm} = 600 K

Next, we discuss a mean Curie temperature T_{cm} = 600 K rather than T_{cm} = 700 K.

Figure 10 (a) shows the bER dependence on H_w for a 2×2 grain arrangement. Although the minimum anisotropy constant ratio K_u/K_{bulk} for 10 years of archiving is 0.27 as shown in Fig. 2, K_u/K_{bulk} = 0.35 is necessary for a low bER. However, a bER less than 10^{-3} cannot be achieved even for $\partial T/\partial x$ = 20 K/nm.

The results for a 3×3 grain arrangement are shown in Fig. 10 (b). A large K_u/K_{bulk} value of 0.75 is necessary for 10 years of archiving. A bER less than 10^{-3} can be achieved for $\partial T/\partial x$ = 20 K/nm.

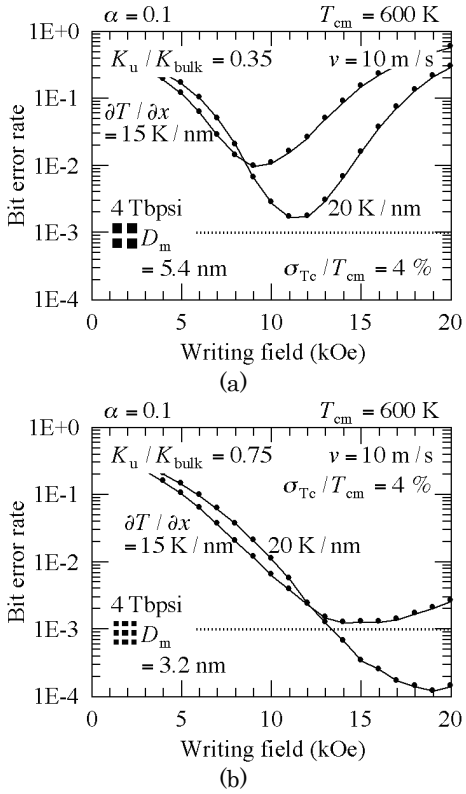

Fig. 10 Dependence of bit error rate on writing field for thermal gradients $\partial T/\partial x$ = 15 and 20 K/nm (α = 0.1, T_{cm} = 600 K, (a) 2×2 and (b) 3×3 grain arrangements).

We summarize the writing field H_w required for the damping constant α = 0.1 in Table 2. A recording density of 4 Tbpsi is available for a linear velocity v = 10 m/s under the conditions used in this study. When the mean Curie temperatures T_{cm} = 700 K, 2×2 (the mean grain size D_m = 5.4 nm) and 3×3 (D_m = 3.2 nm) are necessary for the standard deviations of the Curie temperature σ_{Tc}/T_{cm} = 0 % and 4 %, respectively. Although the minimum anisotropy constant ratios K_u/K_{bulk} for 10 years of archiving are 0.19 and 0.52, the K_u/K_{bulk} values necessary for bER < 10^{-3} are 0.35 and 0.52 for σ_{Tc}/T_{cm} = 0 % and 4 %,

respectively. Furthermore, a larger thermal gradient $\partial T/\partial x$ of 20 K/nm is necessary for σ_{Tc}/T_{cm} = 4 %. In summary, H_w > 8 and 12 kOe are necessary for σ_{Tc}/T_{cm} = 0 % and 4 %, respectively.

When T_{cm} = 600 K, a K_u/K_{bulk} of 0.75, which is larger than that of 0.52 for T_{cm} = 700 K, is necessary for σ_{Tc}/T_{cm} = 4 % due to a low T_{cm} (see Fig. 2).

Table 2 Writing field H_w required for damping constant α = 0.1.

α	0.1			
Recording density (Tbpsi)	4			
T_{cm} (K)	700		600	
σ_{Tc}/T_{cm} (%)	0	4	0	4
$m \times n$ (grains/bit)	2×2	3×3	2×2	3×3
D_m (nm)	5.4	3.2	5.4	3.2
K_u/K_{bulk} for $K_uV_m/kT > 60$	> 0.19	> 0.52	> 0.27	> 0.75
K_u/K_{bulk} for bER < 10^{-3}	0.35	0.52	0.35	0.75
v (m/s)	10	10	10	10
$\partial T/\partial x$ (K/nm)	15	20	15	20
H_w (kOe)	> 8	> 12	> 8	> 13

3.4 α = 0.01

In this section, we discuss a damping constant α = 0.01 instead of α = 0.1. In previous papers[5,7], we have shown that if α is small, WE is dominant and writing is difficult since the attempt period is long and there is almost no opportunity for writing. Since WE is dominant, we used a slow linear velocity v of 5 m/s.

Figures 11 (a) and (b) show the bER dependence on H_w for 3×3 and 4×4 grain arrangements, respectively, where T_{cm} = 700 K. A larger $\partial T/\partial x$ of 20 K/nm is necessary in both cases. With the 4×4 grain arrangement, a higher H_w is necessary since a larger K_u/K_{bulk} is required for 10 years of archiving. The results for T_{cm} = 600 K are shown in Fig. 12 where the same tendency can be seen.

We also summarize the writing field H_w required for the damping constant α = 0.01 in Table 3. A recording density of only 2 Tbpsi is available even for a linear velocity v = 5 m/s under the conditions used in this study since writing is difficult. The grain arrangement and the anisotropy constant ratio K_u/K_{bulk} are 3×3 (the mean grain size D_m = 5.0 nm) and about 0.3, respectively, regardless of the mean Curie temperature T_{cm} and the standard deviation of the Curie temperature σ_{Tc}/T_{cm}. A larger thermal gradient $\partial T/\partial x$ of 20 K/nm is necessary for σ_{Tc}/T_{cm} = 4 %. In summary, H_w > 12 and 14 kOe are needed for σ_{Tc}/T_{cm} = 0 % and 4 %, respectively.

To solve the small α problem it may be effective to use an exchange-coupled composite medium with a large α layer and a large K_u/K_{bulk} layer.

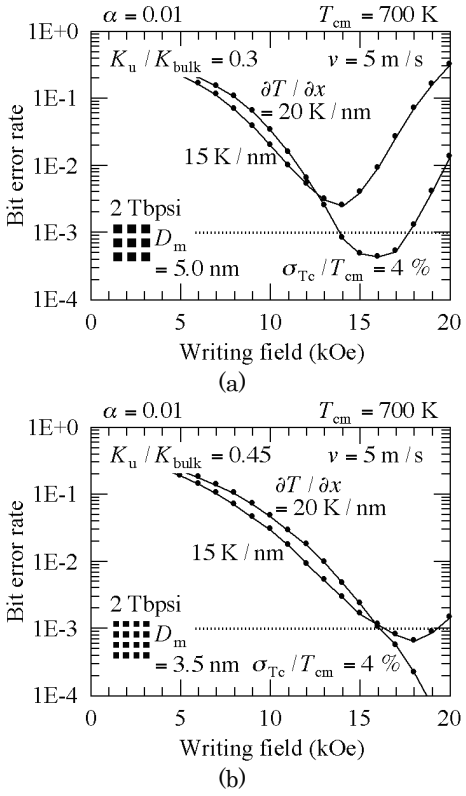

Fig. 11 Dependence of bit error rate on writing field for thermal gradients $\partial T/\partial x$ = 15 and 20 K/nm (α = 0.01, T_{cm} = 700 K, (a) 3×3 and (b) 4×4 grain arrangements).

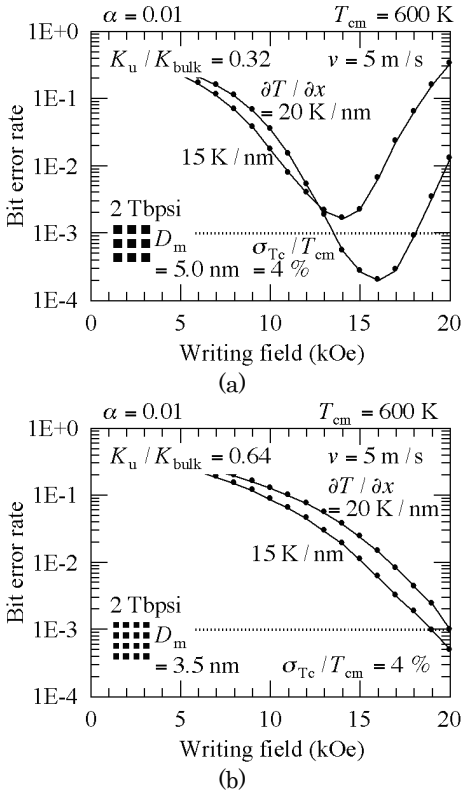

Fig. 12 Dependence of bit error rate on writing field for $\partial T/\partial x$ = 15 and 20 K/nm (α = 0.01, T_{cm} = 600 K, (a) 3×3 and (b) 4×4 grain arrangements).

Table 3 Writing field H_w required for damping constant α = 0.01.

α	0.01			
Recording density (Tbpsi)	2			
T_{cm} (K)	700		600	
σ_{Tc}/T_{cm} (%)	0	4	0	4
$m \times n$ (grains / bit)	3 × 3	3 × 3	3 × 3	3 × 3
D_m (nm)	5.0	5.0	5.0	5.0
K_u / K_{bulk} for $K_u V_m / kT > 60$	> 0.22	> 0.22	> 0.32	> 0.32
K_u / K_{bulk} for bER < 10^{-3}	0.3	0.3	0.32	0.32
v (m / s)	5	5	5	5
$\partial T / \partial x$ (K / nm)	15	20	15	20
H_w (kOe)	> 12	> 14	> 12	> 14

4. Conclusion

We used our simplified model calculation to discuss the Curie temperature T_c variation problem in heat-assisted magnetic recording. The T_c variation increased both write-error (WE) and erasure-after-write (EAW). Increasing the grain column number in one bit was effective in reducing WE and EAW caused by the T_c variation. Furthermore, increasing the thermal gradient for the down-track direction was necessary since EAW was high. A higher writing field of 12 to 14 kOe was necessary when the standard deviation of the Curie temperature σ_{Tc}/T_{cm} = 4 %.

When the damping constant α was 0.1, a recording density of 4 Tbpsi was available for a linear velocity v = 10 m/s under the conditions used in this study even though σ_{Tc}/T_{cm} = 4 %. When the mean Curie temperature T_{cm} = 600 K, a larger anisotropy constant ratio of 0.75 than that of 0.52 for T_{cm} = 700 K was necessary due to a low T_{cm}.

When α = 0.01, WE is dominant and writing is difficult. Therefore, it is necessary to lower v. A recording density of 2 Tbpsi was available for v = 5 m/s and σ_{Tc}/T_{cm} = 4 % under the conditions used in this study.

Acknowledgement We acknowledge the support of the Advanced Storage Research Consortium (ASRC), Japan.

References

1) S. H. Charap, P. -L. Lu, and Y. He: *IEEE Trans. Magn.*, **33**, 978 (1997).
2) T. Kobayashi, F. Inukai, K. Enomoto, and Y. Fujiwara: *J. Magn. Soc. Jpn.*, **41**, 1 (2017).
3) T. Kobayashi, Y. Nakatani, F. Inukai, K. Enomoto, and Y. Fujiwara: *J. Magn. Soc. Jpn.*, **41**, 52 (2017).
4) T. Kobayashi, Y. Nakatani, K. Enomoto, and Y. Fujiwara: *J. Magn. Soc. Jpn.*, **42**, 15 (2018).
5) T. Kobayashi, Y. Nakatani, and Y. Fujiwara: *J. Magn. Soc. Jpn.*, **42**, 127 (2018).
6) J. -G. Zhu and H. Li: *IEEE. Trans. Magn.*, **49**, 765 (2013).
7) T. Kobayashi, Y. Nakatani, and Y. Fujiwara: *J. Magn. Soc. Jpn.*, **42**, 110 (2018).
8) H. Li and J. -G. Zhu: *J. Appl. Phys.*, **115**, 17B744 (2014).
9) T. Kobayashi, Y. Isowaki, and Y. Fujiwara: *J. Magn. Soc. Jpn.*, **39**, 8 (2015).
10) T. Kobayashi, Y. Isowaki, and Y. Fujiwara: *J. Magn. Soc. Jpn.*, **40**, 28 (2016).
11) J. -U. Thiele, K. R. Coffey, M. F. Toney, J. A. Hedstrom, and A. J. Kellock: *J. Appl. Phys.*, **91**, 6595 (2002).
12) T. Ono, H. Nakata, T. Moriya, N. Kikuchi, S. Okamoto, O. Kitakami, and T. Shimatsu: *Appl. Phys. Express*, **9**, 123002 (2016).
13) M. Mansuripur, and M. F. Ruane: *IEEE Trans. Magn.*, **MAG-22**, 33 (1986).

Received Dec. 2, 2018; Accepted Apr. 16, 2019

J. Magn. Soc. Jpn., **43**, 79-83 (2019)

<Paper>

Fabrication of $L1_0$-FeNi films by denitriding FeNiN films

Keita Ito[*,**], Masahiro Hayashida[*], Masaki Mizuguchi[*,**], Takashi Suemasu[***], Hideto Yanagihara[***], and Koki Takanashi[*,**]

[*]Institute for Materials Research, Tohoku Univ., *2-1-1 Katahira, Aoba-ku, Sendai 980-8577, Japan*

[**]Center for Spintronics Research Network, Tohoku Univ., *2-1-1 Katahira, Aoba-ku, Sendai 980-8577, Japan*

[***]Institute of Applied Physics, Univ. of Tsukuba, *1-1-1 Tennodai, Tsukuba, Ibaraki 305-8573, Japan*

$L1_0$-FeNi films textured with the *a*-axis perpendicular to the film plane were successfully fabricated by denitriding FeNiN films. 20-nm-thick FeNiN films with two variants were epitaxially grown on $SrTiO_3$(001), $MgAl_2O_4$(001), and MgO(001) substrates by molecular beam epitaxy. Denitriding was performed by annealing at 300 °C for 4 h under an H_2 gas atmosphere. The epitaxial relationships were $L1_0$-FeNi[001](100) || substrate[100](001) and $L1_0$-FeNi[010](100) || substrate[100](001). The uniaxial magnetic anisotropy energy (K_u) of the $L1_0$-FeNi film was estimated to be 4.4×10^6 erg/cm^3 at room temperature by magnetic torque measurement. This K_u value corresponds to a degree of long range order of 0.4.

Keywords: $L1_0$-FeNi, FeNiN, denitriding, molecular beam epitaxy, uniaxial magnetic anisotropy energy

1. Introduction

According to an increasing demand of a permanent magnet for a motor of next-generation electric vehicles, ferromagnetic materials possessing large uniaxial magnetic anisotropy energy (K_u) and composed of earth abundant elements are required. We have focused on the $L1_0$-ordered FeNi alloy as a rare-earth- and noble metal-free high K_u ferromagnetic material.[1] $L1_0$-FeNi possesses face centered tetragonal structure with alternate stacking of Fe and Ni monatomic layers along the *c*-axis as shown in Fig. 1(a). Lattice constants are a = 3.582 Å and c = 3.607 Å; the c/a ratio is 1.007.[2] Saturation magnetization (M_S) is 1270 emu/cm^3 [3] and the Curie temperature is higher than 550 °C.[4,5] The K_u value was reported to be 1.3×10^7 erg/cm^3 in a bulk sample, [3,6] and 7.0×10^6 erg/cm^3 in a film prepared by molecular beam epitaxy (MBE).[7] We consider that these features of $L1_0$-FeNi are suitable for application to a permanent magnet. However, the order-disorder transition temperature of $L1_0$-FeNi is very low (320 °C),[3,8] and it is difficult to form the $L1_0$ structure by a conventional annealing for FeNi alloys. Atomic diffusion of Fe and Ni is quite slow below 320 °C, and we need an astronomical long duration to obtain $L1_0$-ordered FeNi structure by simple annealing. The formation of bulk $L1_0$-FeNi was realized by several methods, promoting the atomic diffusion of Fe and Ni. For example, introduction of defects in FeNi alloys by neutron irradiation[3,6] or electron bombardment[8] followed by annealing with an external magnetic field, severe plastic deformation technique for FeNi powder,[9] and annealing of rapidly quenched amorphous FeNiSiBPCu alloy.[10] On the other hand, $L1_0$-FeNi films were prepared by alternate monatomic layer deposition using MBE[1,7] or sputtering followed by annealing,[1,11,12]. Although a lot of studies on the formation of $L1_0$-FeNi were made, the degree of long-range order S or the volume fraction of $L1_0$-FeNi phase was not enough. Recently, however, the synthesis of polycrystalline $L1_0$-FeNi powder with large S (0.71) has been achieved by nitrogen topotactic extraction from FeNiN powder.[13] Figure 1(b) shows the crystal structure of FeNiN. FeNiN possesses a similar crystal stricture to that of $L1_0$-FeNi, and thermodynamically stable ordered structure of FeN and Ni layers.[14] Actually, the polycrystalline FeNiN powder with large S was formed by a simple nitridation method for $A1$-FeNi (Fe and Ni are randomly located) powder using NH_3 gas.[13] The $L1_0$-FeNi powder was formed by denitriding FeNiN by annealing under H_2 gas atmosphere. However, the evaluation of its K_u value has never been performed because of polycrystalline powder. In this study, we have tried to grow epitaxial FeNiN films on $SrTiO_3$(STO)(001), $MgAl_2O_4$(MAO)(001), and MgO(001) substrates by molecular beam epitaxy (MBE), and fabricated $L1_0$-FeNi films with two variants by denitriding FeNiN films.

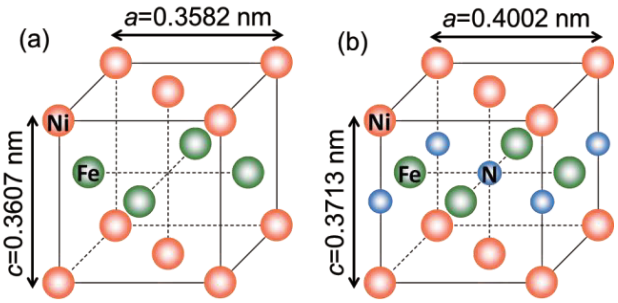

Fig. 1 Crystal structure of (a) $L1_0$-FeNi and (b) FeNiN.

2. Experiment

20 nm-thick FeNiN films were grown on STO(001), MAO(001), and MgO(001) substrates by MBE in an

ultra-high vacuum chamber supplying Fe, Ni, and radio-frequency (RF) N_2 plasma, simultaneously.[15] The lattice mismatches in the *c* plane between FeNiN and the substrates are 2.5 (STO), –0.98 (MAO), and –4.9 % (MgO). Supply rates of Fe and Ni were controlled to get the equiatomic composition of Fe and Ni. The growth temperature, N_2 gas flow rate, and RF input power were fixed to be 300 °C, 1.0 sccm, and 240 W, respectively. Then, denitriding was performed by furnace annealing at 300 °C for 4 h under H_2 gas flow rate of 1 L/min at ambient pressure. Structure of the samples was characterized by out-of-plane (ω-2θ) and in-plane (φ-$2\theta_\chi$) x-ray diffraction (XRD) using Cu-$K\alpha$ radiation. The thickness of the $L1_0$-FeNi layer was estimated by x-ray reflectometry (XRR). Magnetization curves were measured by vibrating sample magnetometer at room temperature (RT). Magnetic field was applied to in-plane or out-of-plane direction of the films. The K_u value was estimated by a magnetic torque (L) measurement with a 45°-torque method.[16] Torque curves were measured at RT under the applied field in the range of 2 to 19 kOe by rotating the electromagnet clockwise and counterclockwise around the (010)-plane of the substrates.

3. Results and discussion

Figure 2(a) shows the ω-2θ XRD patterns of the FeNiN films. Only the diffraction peak of FeNiN 200 is observed, and the *a*-axes of FeNiN films are perpendicular to the film plane for all the substrates. Figures 2(b) and 2(c) show the φ-$2\theta_\chi$ XRD patterns of the same samples. The scattering vector ($\boldsymbol{Q}$) was set to the [100] direction of the substrates. In Fig. 2(b), the peaks of FeNiN 020 and 002 are obtained. This means that the FeNiN films are epitaxially grown with two variants: the epitaxial relationships are

FeNiN[001](100) | | STO, MAO, MgO[100](001) and

FeNiN[010](100) | | STO, MAO, MgO[100](001),

as shown schematically in Fig. 3. There are the two variants with the in-plane *c*-axis of FeNiN intersecting at 90°. In Fig. 2(c), the super lattice peak of FeNiN 001 is clearly observed for all the samples. This is attributed to the long-range order of N atoms in the FeNiN films.[15]

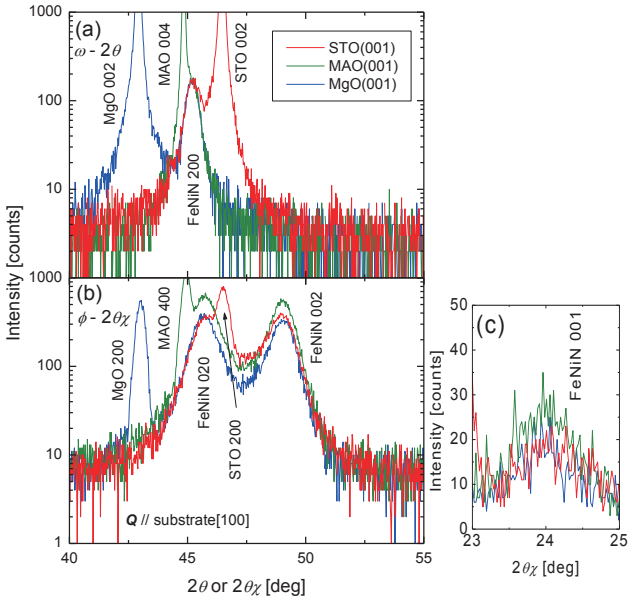

Fig. 2 (a) ω-2θ and (b)(c) φ-$2\theta_\chi$ XRD patterns of samples.

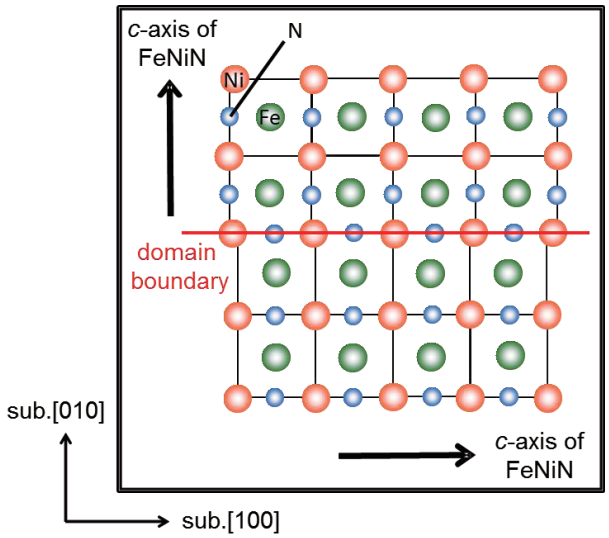

Fig. 3 Epitaxial relationship between FeNiN layer and substrate.

Figures 4(a) and 4(b) show the XRR patterns of the sample grown on the STO(001) substrate before and after the denitriding process, respectively. The red and blue curves correspond to the experiments and the calculations based on the models shown in the right-hand figures, respectively. After denitriding, the

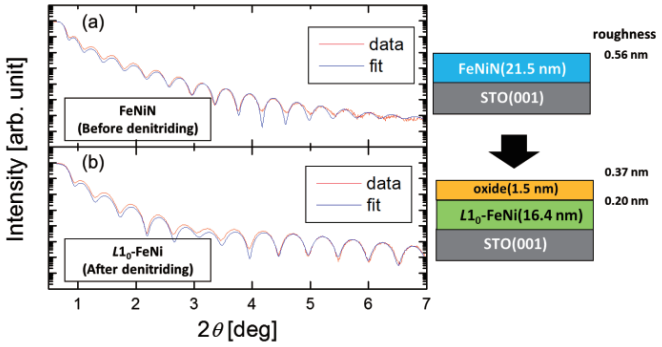

Fig. 4 XRR patterns of FeNiN/STO(001) (a) before and (b) after denitriding.

calculated curve assuming the existence of the surface oxidation layer agrees well to the experiment. The total film thickness becomes thinner after denitriding. This is attributed to the shrink of the unit-cell volume associated with the change from FeNiN to $L1_0$-FeNi.

Figures 5(a) and 5(b) show the ω-2θ and φ-$2\theta_\chi$ XRD patterns of the denitrided samples, respectively. The dashed lines indicate the peak position of $L1_0$-FeNi 002 and 200 expected from the lattice constants of bulk $L1_0$-FeNi. The diffraction around $2\theta = 52°$ in Fig. 5(a) corresponds to $L1_0$-FeNi 200, and that around $2\theta_\chi = 51°$ in Fig. 5(b) is associated with $L1_0$-FeNi 002 and 020. The peak shift from the dashed lines indicates the tensile strain induced in the films by the larger lattice constants of substrates than that of $L1_0$-FeNi. Therefore, we can say that the epitaxial relationship between the $L1_0$-FeNi films and the substrates is maintained after the denitriding process as shown in Fig. 6:

$L1_0$-FeNi[001](100) || STO, MAO, MgO[100](001) and

$L1_0$-FeNi[010](100) || STO, MAO, MgO[100](001).

Fig. 7(a) and 7(b) display the magnetization curves of the $L1_0$-FeNi films in the in-plane ([100] of the substrates) and out-of-plane magnetic fields, respectively. M_S of the samples are approximately 1100 emu/cm^3 for all the samples. For comparison an epitaxially grown A1-FeNi film was prepared on STO(001) and the magnetization curves were measured as shown by black ones in Figs. 7(a) and 7(b). In Fig. 7(a), the $L1_0$-FeNi films formed by denitriding show

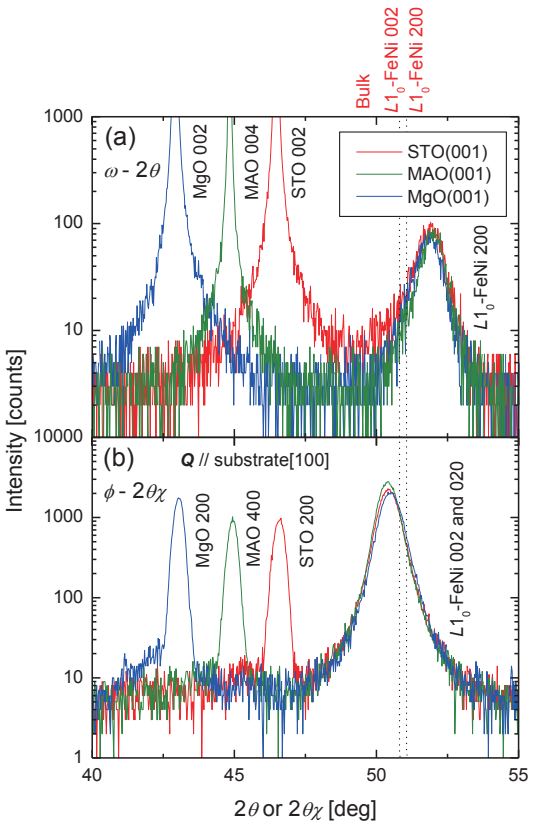

Fig. 5 (a) ω-2θ and (b) φ-$2\theta_\chi$ XRD patterns of denitrided samples.

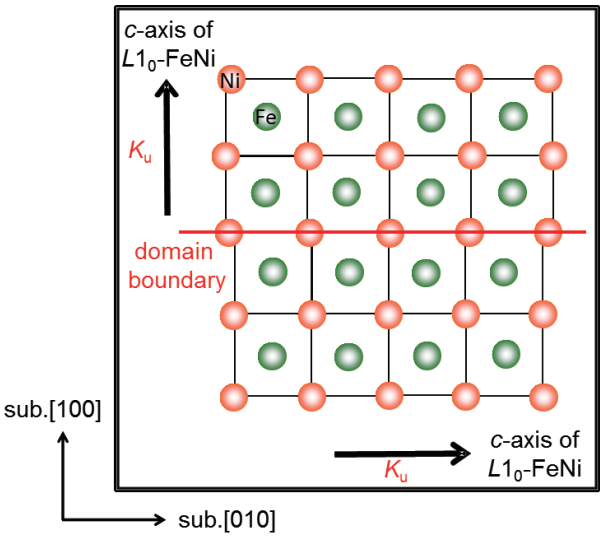

Fig. 6 Epitaxial relationship between $L1_0$-FeNi layer and substrate.

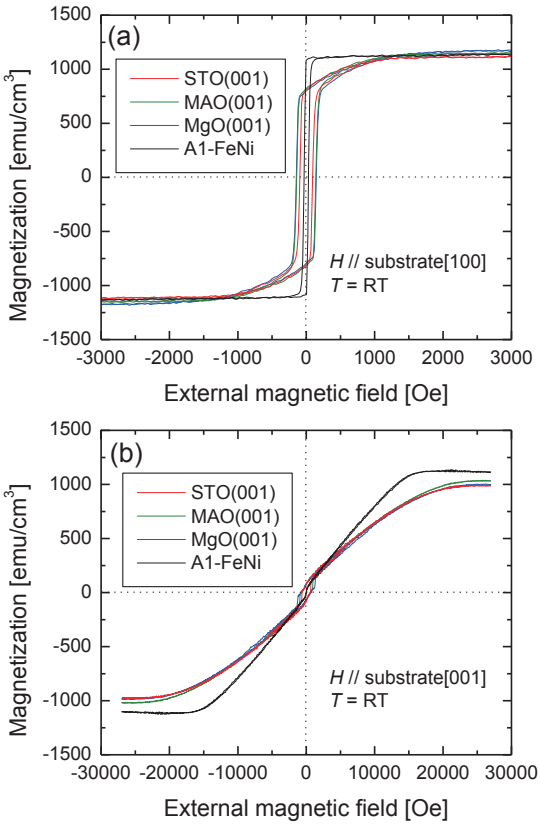

Fig. 7 Magnetization curves of $L1_0$-FeNi films when magnetic field was applied to (a) in-plane and (b) out-of-plane directions of films.

larger coercive fields and smaller remanent magnetizations than those of the A1-FeNi film. This is attributed to the presence of the *a*-axis (magnetic hard axis) of $L1_0$-FeNi along to the in-plane direction of the denitrided samples, as shown in Fig. 6. Furthermore, in Fig. 7(b), the saturation fields of denitrided $L1_0$-FeNi films are larger than that of the A1-FeNi film. This is explained by the *a*-axis (magnetic hard axis) orientation of $L1_0$-FeNi perpendicular to the film plane in the denitrided samples. These results strongly suggest the formation of *a*-axis textured $L1_0$-FeNi films which have two variants with different *c*-axis directions from each other, showing uniaxial magnetic anisotropy for each. There is no significant difference in structure and magnetic properties of the denitrided samples grown on the three different substrates.

Figure 8 shows the torque curves of the $L1_0$-FeNi film on STO(001). The inset shows the geometry of the film sample and the magnetic field. θ is the angle relative to the surface normal: θ = 90° and θ = 0° show that the magnetic field was applied in parallel to the in-plane and out-of-plane of the $L1_0$-FeNi film, respectively. The saw-tooth-like curves show that the magnetization is not saturated at 19 kOe. These curves exhibit two-hold symmetry because of K_u in the $L1_0$-FeNi film. Figure 9 shows the L - $(L/H)^2$ plots using the averaging absolute values at θ = 45°, 135°, 225°, and 315°. The M_S and

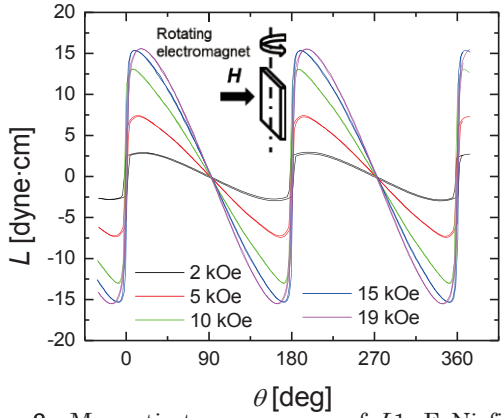

Fig. 8 Magnetic torque curves of $L1_0$-FeNi film on STO(001).

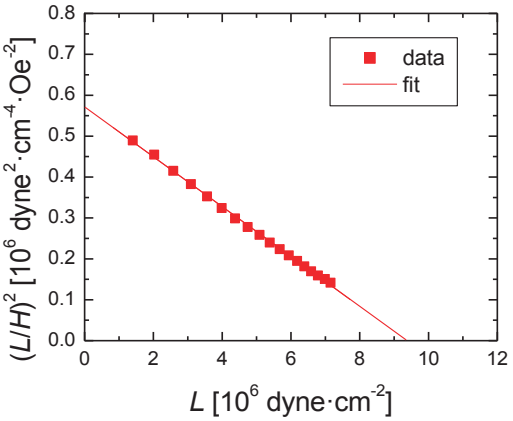

Fig. 9 L - $(L/H)^2$ plots for $L1_0$-FeNi film on STO(001).

effective uniaxial magnetic anisotropy energy (K_u^{eff}) values were obtained from the intersections of the fitting lines with the vertical and horizontal axes, respectively. By considering the two variants of the sample, magnetic anisotropy energy (E_A) and L are expressed by equations (1) and (2), respectively.

$$E_A = 1/2\cdot(K_u + 2\pi M_S^2)\cdot\sin^2\theta + 1/2\cdot 2\pi M_S^2\cdot\sin^2\theta \quad (1)$$

$$L = -dE_A/d\theta = -(K_u/2 + 2\pi M_S^2)\cdot\sin 2\theta \quad (2)$$

Here, it is noted that positive K_u means the easy magnetization axis in the in-plane direction. Using the equation $K_u^{eff} = K_u/2 + 2\pi M_S^2$, the K_u value is calculated to be 4.4×10^6 erg/cm^3 for $L1_0$-FeNi/STO(001). From the relationship between K_u and S reported for $L1_0$-FeNi films prepared by MBE,[7] K_u of 4.4×10^6 erg/cm^3 corresponds to S of 0.4. This value is smaller than that of the $L1_0$-FeNi powder reported in ref. 13 (S = 0.71). In our case, denitriding was performed at 300 °C, which is higher than that in ref. 13 (250 °C). We chose higher temperature to promote denitriding. However, this high temperature might have caused the deterioration of the $L1_0$ structure and the reduction of S and K_u, when the N atoms were extracted from the FeNiN lattice. Further optimization of the denitriding conditions and the elucidation of the denitriding mechanism are required in order to obtain much larger S and K_u values.

4. Summary

We have succeeded in growing *a*-axis textured FeNiN films with the two variants on STO(001), MAO(001), and MgO(001) substrates by MBE, and forming $L1_0$-FeNi films by denitriding them. The K_u of the $L1_0$-FeNi film is estimated to be 4.4×10^6 erg/cm^3 at RT, and the S is expected to be approximately 0.4. In ordered to get higher S and K_u, as a next step, the optimization of the growth conditions and denitriding conditions of the FeNiN films are required.

Acknowledgements This work was supported in part by the Elements Strategy Initiative Center for Magnetic Materials (ESICMM) under the outsourcing project of Ministry of Education, Culture, Sports, Science and Technology, Japan. The XRD measurements were carried out at the Cooperative Research and Development Center for Advanced Materials, IMR, Tohoku University. The magnetic torque curve measurements were performed with the help of T. Sekido, the University of Tsukuba. We thank S. Goto and H. Kura, DENSO CORPORATION, for fruitful discussion about the denitriding process.

References

1) K. Takanashi, M. Mizuguchi, T. Kojima, and T. Y. Tashiro: *J. Phys. D: Appl. Phys.*, **50**, 483002 (2017).
2) M. Kotsugi, H. Maruyama, N. Ishimatsu, N. Kawamura, M.

Suzuki, M. Mizumaki, K. Osaka, T. Matsumoto, T. Ohkochi, and T. Ohtsuki: *J. Phys.: Condens. Matter*, **26**, 064206 (2014).
3) J. Paulevé, A. Chamberod, K. Krebs, and A. Bourret: *J. Appl. Phys.*, **39**, 989 (1968).
4) T. Nagata and M. Funaki: *Mem. Natl Inst. Polar Res. Spec.*, **46**, 245 (1987).
5) P. Wasilewski: *Phys. Earth Plan. Inter.*, **52**, 150 (1988).
6) L. Néel, J. Paulevé, R. Pauthenet, J. Laugier, and D. Dautreppe: *J. Appl. Phys.*, **35**, 873 (1964).
7) T. Kojima, M. Mizuguchi, T. Koganezawa, K. Osaka, M. Kotsugi, and K. Takanashi: *Jpn. J. Appl. Phys.*, **51**, 010204 (2012).
8) K. B. Reuter, D. B. Williams, and J. I. Goldstein: *Met. Trans. A*, **20**, 711 (1989).
9) S. Lee, K. Edalati, H. Iwaoka, Z. Horita, T. Ohtsuki, T. Ohkochi, M. Kotsugi, T. Kojima, M. Mizuguchi, and K. Takanashi: *Phil. Mag. Lett.*, **94**, 639 (2014).
10) A. Makino, P. Sharma, K. Sato, A. Takeuchi Y. Zhang, and K. Takenaka: *Sci. Rep.*, **5**, 16627 (2015).
11) T. Y. Tashiro, M. Mizuguchi, T. Kojima, T. Koganezawa, M. Kotsugi, T. Ohtsuki, K. Sato, T. Konno, and K. Takanashi: *J. Alloys Compd.*, **750**, 164 (2018).
12) A. Frisk, B. Lindgren, S. D. Pappas, E. Johansson, and G. Andersson: *J. Phys.: Condens. Matter.*, **28**, 406002 (2016).
13) S. Goto, H. Kura, E. Watanabe, Y. Hayashi, H. Yanagihara, Y. Shimada, M. Mizuguchi, K. Takanashi, and E. Kita: *Sci. Rep.*, **7**, 13216 (2017).
14) R. J. Arnott and A. Wold: *J. Phys. Chem. Solids*, **15**, 152 (1960).
15) F. Takata, K. Ito, and T. Suemasu: *Jpn. J. Appl. Phys.*, **57**, 058004 (2018).
16) H. Miyajima, K. Sato, and T. Mizoguchi: *J. Appl. Phys.*, **47**, 4669 (1976).

Received Jan. 18, 2019; Accepted Apr. 16, 2019

J. Magn. Soc. Jpn., **43**, 84-90 (2019)

<Paper>

Suppression of Heat Generation in Magnetic Stimulation Coil Applied for Treating Dysphagia

H. Mori[*,**], H. Kagaya[***], S. Izumi[****], K. Yashima[*], and T. Takagi[*****]

[*]IFG Corporation, *1-14-9 Oritate, Aoba-ku, Sendai 982-0261, Japan*
[**]Graduate School of Engineering, Tohoku Univ., *6-6 Aramaki aza aoba, Aoba-ku, Sendai 980-8579, Japan*
[***]Department of Rehabilitation Medicine I, School of Medicine, Fujita Health Univ.
1-98 Dengakugakubo, Kutsukake-cho, Toyoake, Aichi, 470-1192 Japan
[****]Graduate School of Biomedical Engineering, Tohoku Univ., *2-1 Seiryo-machi, Aoba-ku, Sendai, 980-8575 Japan*
[*****]Institute of Fluid Science, Tohoku Univ., *2-1-1 Katahira, Aoba-ku, Sendai, 980-8577 Japan*

The authors are developing magnetic stimulation coils for use in the treatment of dysphagia. The prototype coil manufactured in our previous research can induce large contraction of the suprahyoid muscles, which should be trained for normal swallowing. In this study, the heat generation in the coil during magnetic stimulation is investigated and suppressed. A numerical analysis showed that the main cause of the generated heat is the eddy current in the coil conductor induced by magnetic flux from the tip of the magnetic core. The analysis also showed that a parallel coil with a cross connection has an ideal current distribution in the coil conductor and thus best suppresses heat generation during magnetic stimulation. The heat-suppressing coil has parallel divided coil conductors and an appropriate connection between the conductors to level the current in each conductor. Moreover, measurements of the temperature rise in prototype coils during magnetic stimulation confirm that heat generation can be greatly suppressed by dividing the conductor and using an appropriate connection between the divided conductors.

Key words: magnetic stimulation, dysphagia, suprahyoid muscles, eddy current, parallel coil

1. Introduction

Dysphagia, or difficulty swallowing, is mainly caused by cerebrovascular disorders and aging. In Japan, a super-aging society, the number of people with dysphagia is rapidly increasing. When food enters the trachea or bronchi due to inappropriate swallowing motion, it can cause aspiration pneumonia[1,2]. Pneumonia is the 3rd leading cause of death in Japan. More than 70% of pneumonia cases in elderly people are related to aspiration[3]. Recovery from dysphagia is thus important for protecting the elderly.

Neuromuscular electrical stimulation (NMES), a stimulation method that uses electrodes that are stacked directly on the epidermis above swallowing-related muscles such as the suprahyoid muscles, has recently been used for the treatment of dysphagia. Several studies have shown that treatment with NMES promotes swallowing recovery[4,5]. NMES is frequently recommended by therapists in the United States [6]. However, when NMES is applied to the suprahyoid muscles using an intensity that does not cause pain or discomfort, the induced contraction of muscles is smaller than that in usual swallowing[7,8]. This occurs because the current intensity required to stimulate the motor point of the suprahyoid muscles deep below the epidermis is also sufficient to stimulate nociceptors just under the epidermis. In addition, it is difficult to adhere electrodes to the lower jaw epidermis of the elderly because of slack skin, leading to insufficient electrical contact. Moreover, for men, beards make electrode contact more difficult.

To overcome these problems, a method that uses magnetic stimulation has been proposed[9,10]. Magnetic stimulation excites motor nerves via a current induced by rapid changes of the magnetic flux of a coil; this current induces contraction of the target muscle. Magnetic stimulation only slightly stimulates nociceptors, so there is little pain or discomfort during stimulation[11]. Moreover, contact with skin is unnecessary for stimulation, so beards and slack skin do not cause problems. In our previous studies, numerical analysis showed that a coil with a U-shaped magnetic core (U-core coil hereafter) is the most suitable coil for stimulating the motor point of the suprahyoid muscles[12]. The figure-8 coil developed by Ueno is widely known for local magnetic stimulation [13]. A U-core coil consists of a figure-8 coil and a magnetic core. It focuses a strong magnetic flux to stimulate the motor point of the suprahyoid muscles but not the lower alveolar nerve. A clinical test on healthy humans confirmed that magnetic stimulation with a U-core coil can induce contraction of the suprahyoid muscles. Figure 1 shows the placement of a coil for stimulating the motor point of the suprahyoid muscles. Contraction of the suprahyoid muscles upon stimulation can be monitored by imaging the movement of the hyoid bone connected to the muscle using X-ray fluoroscopy. Figure 2 shows X-ray fluoroscopy images of the region near the lower jaw before and during stimulation. Upon stimulation, the

Fig. 1 Placement of coil for stimulating the motor point of the suprahyoid muscles.

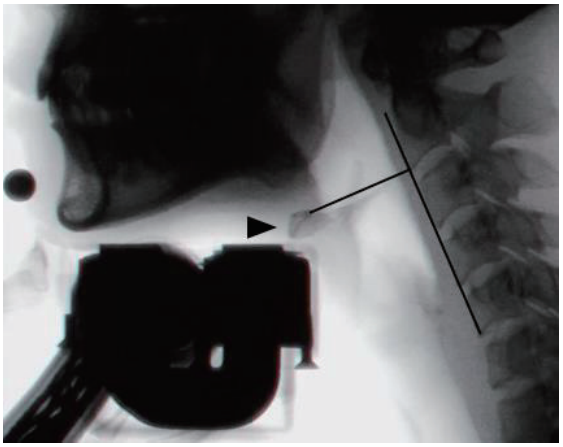

(a)

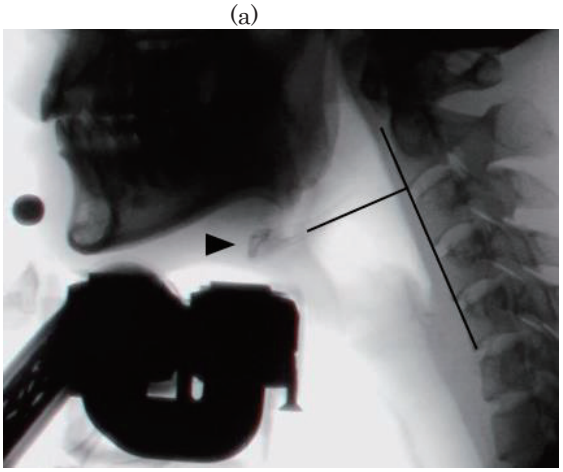

(b)

Fig. 2 Measurement of hyoid bone movement using X-ray fluoroscopy. The shaded region indicated by the black triangle is the hyoid bone. (a) Before and (b) during stimulation.

hyoid bone significantly moved in the anterior and superior directions, indicating that the suprahyoid muscles greatly contracted. It has been shown that a contraction comparable to that in swallowing by a healthy person can be obtained using magnetic stimulation, significantly exceeding that induced by NMES, without great pain or discomfort[14].

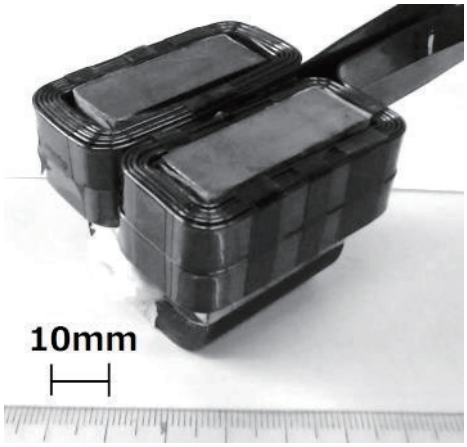

(a)

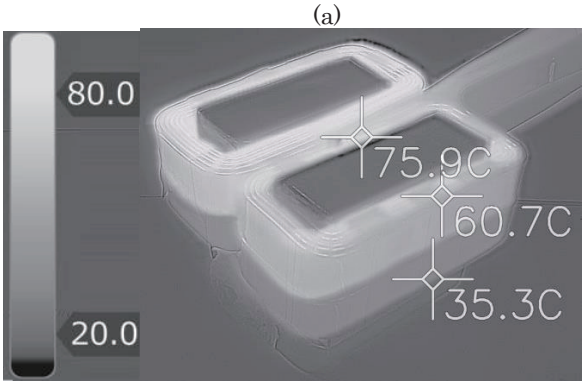

(b)

Fig. 3 (a) External view of magnetic stimulation coil without a coil case. (b) Temperature distribution after the generation of 600 magnetic pulses measured by thermography.

Continuous stimulation using a U-core coil generates heat around the tip of the magnetic core, which increases the temperature of the surface in contact with the patient's skin. In particular, for the small stimulation coil used for patients with a small jaw, because the heat capacity is small (i.e., it is easy to heat), the surface temperature rises to an unsafe value. Fig. 3 shows a thermographic image of the surface of a small coil after 600 continuously generated magnetic pulses. It can be seen that the coil is overheated from the tip side of the magnetic core; the temperature of the coil reaches about 75 °C. Although the coil is covered with a resin cover for insulation, there is a danger of burning the patient via the heat transmitted through the resin cover. The cover itself may also to be damaged by the heat.

In this study, to reduce the temperature of the coil surface during magnetic stimulation, the current density distribution inside the coil during magnetic stimulation is obtained using numerical analysis to clarify the mechanism of heat generation. Based on this information, a method for suppressing heat generation is developed. A temperature test using prototype coils is used to validate the proposed heat suppression method.

2. Numerical Analysis

2.1 Model and conditions

The software ANSYS Electromagnetics Suite 19.1 was used for numerical analysis and Eddy Current Solver was used for AC steady state analysis. For numerical analysis, various coil models were prepared. Figure 4 (a) shows a conventional coil model with the same shape and size as those of a prototype U-core coil. The U-core coil is composed of a U-shaped magnetic core made of a silicon steel sheet and a pair of coils. As shown in Fig. 5 (a), the coils are manufactured by winding an insulated copper flat plate (thickness: 0.9 mm; width: 8 mm) with double pancake winding. This model is denoted as the single-coil model.

We also prepared a model in which the coil conductors are divided to suppress the eddy current (Fig. 4 (b)). The coils are manufactured by winding five flat copper plates (thickness: 0.9 mm; width: 1.6 mm) in parallel. This model is denoted as the parallel-coil model. As shown in Fig. 5 (b), the coils wound around one tip of the core are denoted as A1, A2, ... A5 starting from the layer on the tip side. Similarly, the coils wound around the other tip of the core are denoted as B1, B2, ... B5. For analysis of the parallel coil, two methods for connecting coils were applied. As shown in Fig. 6, one connection method (straight connection) is to connect the coils of a given layer (A1-B1, A2-B2, ... A5-B5). The other connection method (cross connection) is to connect a coil from the tip-side layer to a coil from the base-side layer (A1-B5, A2-B4, ... A5-B1). The parallel-coils with straight and cross connections are denoted as parallel coil (straight) and parallel coil (cross), respectively.

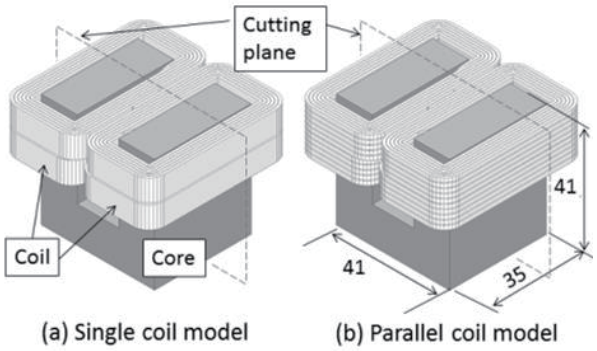

Fig. 4 (a) Single- and (b) parallel-coil models (units: mm).

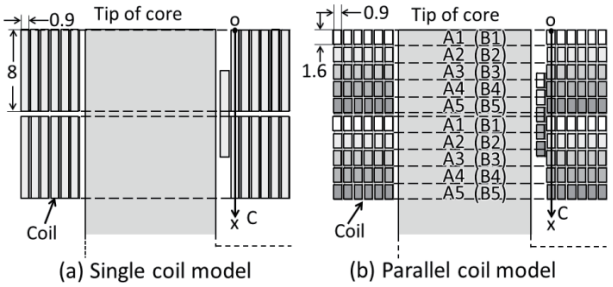

Fig. 5 Partial cross-section views of (a) single- and (b) parallel-coil models along the cutting plane shown in Fig. 4. This figure shows a view near one side of a core tip.

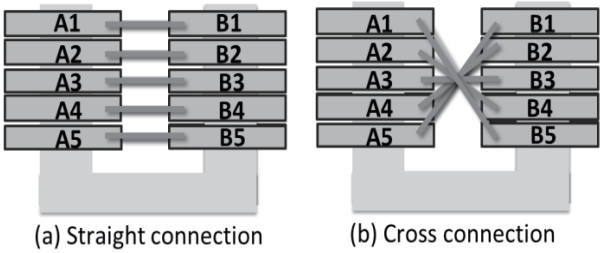

Fig. 6 Methods for connecting coil layers.

The current density distribution in the conductor when a 1.1 kA, 2.35 kHz sinusoidal current is supplied to these coils was analyzed. The value of current is for entire coil not for each coil layer. The current condition was determined by measuring the waveform of the actual current flowing through the prototype coil during magnetic stimulation. The current supplied to a coil used for treatment is an intermittent biphasic pulse. However, the results of an analysis with a continuous sinusoidal current are applicable to coil development[15].

2.2 Results of numerical analysis

Fig. 7 shows the current density distribution inside the conductor of each coil on line C shown in Fig. 5. The current density distribution shown in the figure was obtained at the phase at which the current density inside the conductor was maximum. The level indicated by "Ideal" shows the current density for a current flowing evenly through the conductor.

The results for the single coil in Fig. 7 show that the current density is biased toward the tip side of the core. The current density reaches a value nine times the ideal density. This current density distribution is equivalent to a state in which a current is flowing through a conductor that is thinner than the actual one and the effective resistance of the conductor increases, greatly increasing heat generation. In addition, because Joule heat is proportional to the square of the current density, the region of the coil close to the tip of the core generates particularly strong heat. It is found that the direction of the current density is opposite to that of the supply

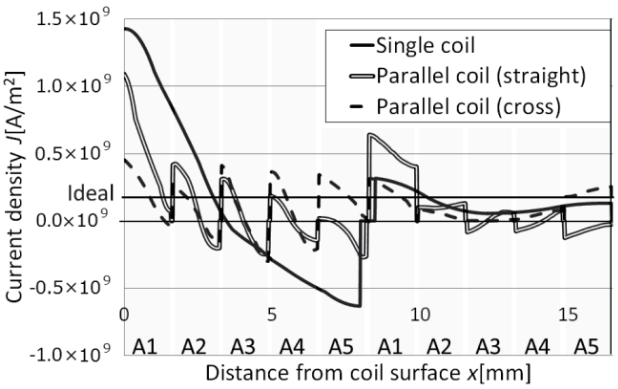

Fig. 7 Current density distribution inside various types of coil during magnetic stimulation.

current in the region of the coil apart from the tip of the core. This opposite current density reduces magnetic flux in the core and generates unnecessary Joule heat. The cause of this bias is considered to be the eddy currents inside the conductor induced by the magnetic flux generated from the tip of the core. Fig. 8 shows a vector diagram of the magnetic flux calculated under a forced condition where eddy current does not occur in the coils. It can be seen that a strong magnetic flux passes through the coil portion between the tips of the core. The induced eddy current flows to cancel out this magnetic flux.

The results for the parallel coil (straight) in Fig. 7 show that the maximum current density is suppressed compared with that for a single coil. This suppression is likely due to the subdivision of the conductor, which interrupts the eddy current flow. More specifically, the current density in the A1 layer is high, and the current flow in the A5 layer is opposite to the supply current. It is considered that the magnetic flux through the coil induces a positive electromotive force in the A1 (B1) layer and a negative electromotive force in the A5 (B5) layer. The eddy current induced by the electromotive force overlaps the current from the current supply, and the current density distribution shown in Fig.7 is appeared. In Fig. 9, the behavior of the eddy current flow in the parallel coil (straight) is simplified and illustrated. In the figure, each layer of coil is expressed as one turn coil to make it easy to understand. All layers of coil are connected in parallel at the points where the pulse current is supplied from a pulse current supply. So there is an eddy current path through A1–B1–B5-A5 layer. Focusing on the surface bordered with the closed curve of the eddy current path, the surface has a large area, and all white arrows that indicate the direction of magnetic flux are incident on same face of the surface. It means that, when a magnetic flux is generated from the core, a large amount of eddy current is induced on the eddy current path. Therefore, the results of this numerical analysis show that it is impossible to sufficiently flatten the deviation of the current density by merely subdividing the conductor.

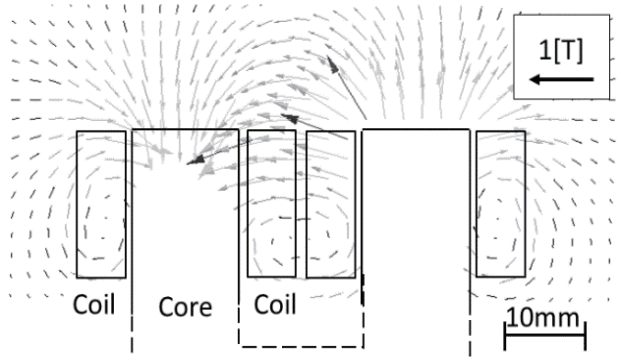

Fig. 8 Vector diagram of magnetic flux on cutting plane under the condition of no eddy current.

Moreover, the results for the parallel coil (cross) in Fig. 7 show that the current density is suppressed to a level close to the ideal distribution. This suppression is likely due to the electromotive force in the A1 (B1) layer, which makes the current flow in the positive direction, and the electromotive force in the B5 (A5) layer, which makes the current flow in the reverse direction; these currents cancel each other out.

Table 1 shows the heat generated by various types of coil after one pulse of magnetic stimulation calculated in the numerical analysis. The values for the single coil, 5.5, and 3.4 J, respectively. Compared to the single coil, heat generation is suppressed by 52% using the parallel coil (cross).parallel coil (straight), and parallel coil (cross) are 7.1,

The results of the numerical analysis show that the main cause of the heat generation in a U-core coil is the eddy current induced inside the coil conductor via the magnetic flux generated from the tip of the core. It was shown that dividing the coil conductor and using a cross connection between coils provides a current density distribution close to the ideal level, suppressing heat generation.

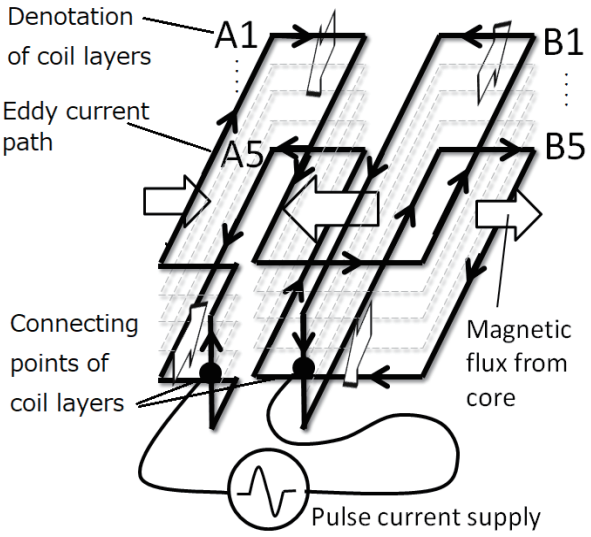

Fig. 9 Simplified eddy current path model for the parallel coil (straight) for eddy current induced by magnetic flux from the core.

Table 1 Solid loss for various types of coil

Coil Model	Quantity of heat generated by 1 pulse (J)
Single Coil (Conventional coil)	7.1
Parallel Coil (Straight)	5.5
Parallel Coil (Cross)	3.4
Ideal Coil (Uniform current density)	1.9

Because the cause of heat generation is an eddy current induced by the magnetic flux passing through the coil, heat generation could be reduced by suppressed the eddy current using litz wire manufactured by twisting a thin enameled wire. However, in general, litz wire has a space factor of about 50% to 60%, and thus it is expected that the effective direct current resistance of the coil will roughly double when litz wire is used. Even if the current of each strand flows evenly and an ideal current distribution is obtained, because heat generation is proportional to the resistance value, it is expected to roughly double. Therefore, it is thought that the heat generation is the same as or greater than that in the parallel coil (cross). In addition, for litz wire, each fine element wire is insulated by a resin coating film, so for the heat inside to be dissipated to the outside, it must pass through several layers of the insulation film. When the temperature rises, it is thus difficult to decrease the temperature inside the coil [16].

3. Temperature Test using Prototype Coils

3.1 Method

The three types of coil used in the numerical analysis were manufactured and their temperature rise was measured. The temperature rise over the entire coil surface was measured using thermography. In addition, two K-type thermocouples were installed at the upper and lower ends of the coil, respectively, and the temperature was recorded with a data logger. The temperature measurement points are shown in Fig. 10.

The conditions for pulse current conduction were set to those that obtain the highest frequency assumed to be used for subjects. Specifically, a cycle in which 30 pulses were generated per second for 2 seconds and then stopped for 2 seconds was repeated. The waveform of each pulse is 1 cycle of sinusoidal wave. The coil surface temperature was measured during the cycle. The supplied pulse current was set so that the amplitude would be 1.10 kA. The value of amplitude was for entire coil not for each coil layer. The pulse current was supplied from a pulse current supply using capacitor discharge. The wavelengths of pulse current were 422-434 μs and the inverses of the wavelengths are equivalent of 2.30-2.38 kHz of frequency.

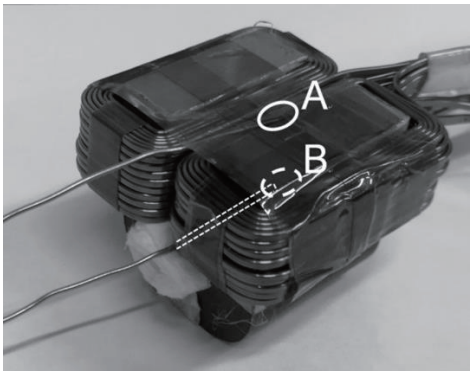

Fig. 10 Temperature measurement points on coil.

In this condition, the magnetic flux densities at 1mm above tip core of single coil, parallel coil (straight), and parallel coil (cross) were 0.92 T, 0.90 T, and 0.93 T, respectively, and that at 16mm above were 0.21 T, 0.21 T, and 0.21 T, respectively. Considering 1mm of the thickness of resin cover for insulation, it means that the magnetic flux density on the patient skin exceeds 0.90T, and that at the region 15mm inward from skin exceeds 0.20 T. Because the amplitude of magnetic flux density over 0.20 T is enough to stimulate nerve [17], these coils can stimulate nerves at depth of 15mm.

The generation of pulses was started after the surface temperature of the coil was confirmed to be about room temperature (22 °C ± 2 °C).

3.2.1 Results of thermography test

Figures 11-13 show thermographic images taken after 600 and 1200 pulses for the three types of coil, respectively.

The experimental results for the single coil (Fig. 11) show large heat generation in the upper coil, which is consistent with the numerical analysis results. In the numerical analysis results, because the current density was strongly concentrated on the tip side of the upper coil, the temperature rise seemed to be also concentrated at the tip side. However, in the experiment, the upper and lower coils almost uniformly increased in temperature, respectively. This is thought to be caused by the coil not being finely divided and the heat being diffused throughout the upper and lower coils because of the high thermal conductivity of copper.

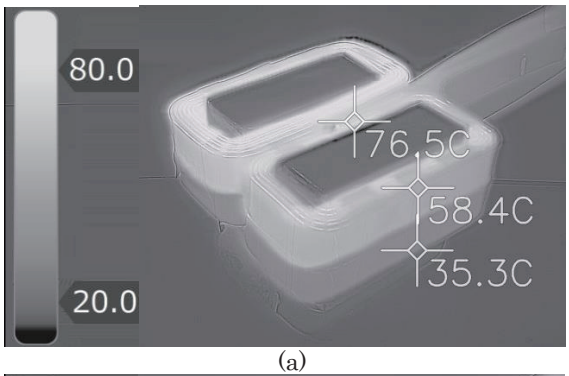

(a)

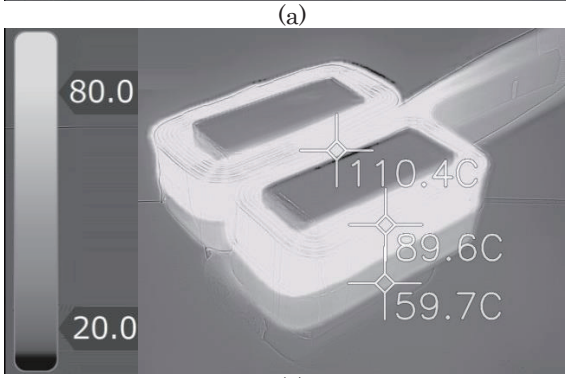

(b)

Fig. 11 Temperature distribution in single coil measured using thermography. Temperature distributions after (a) 600 and (b) 1200 pulses.

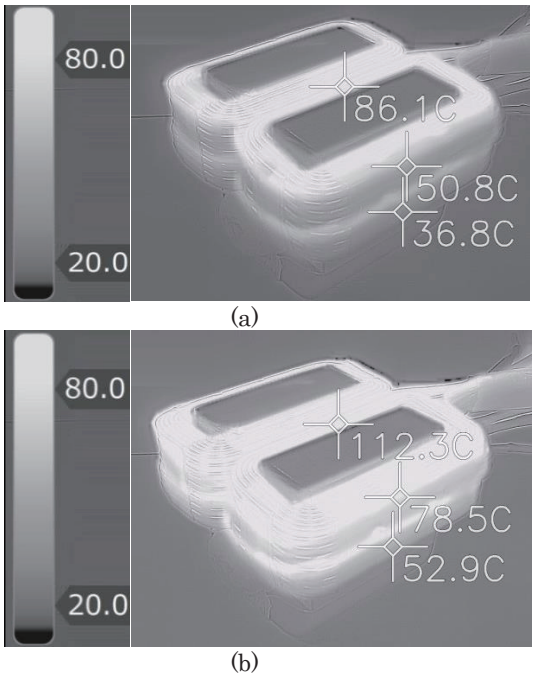

Fig. 12 Temperature distribution in parallel coil (straight) measured using thermography. Temperature distributions after (a) 600 and (b) 1200 pulses.

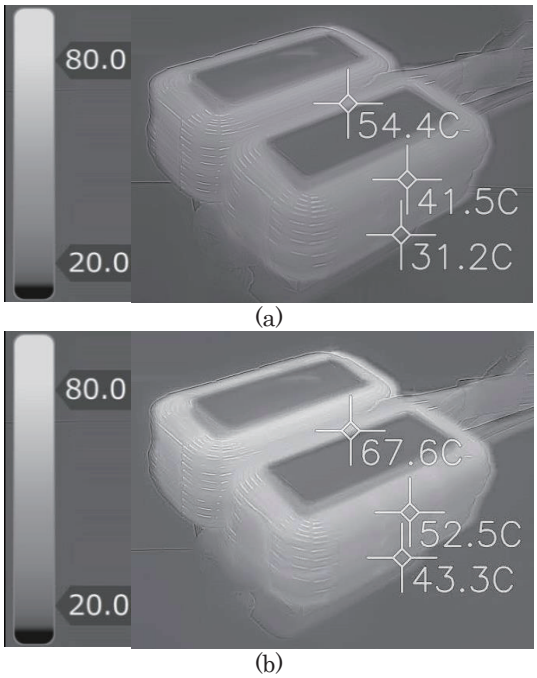

Fig. 13 Temperature distribution in parallel coil (cross) measured using thermography. Temperature distributions after (a) 600 and (b) 1200 pulses.

The experimental results for the parallel coil (straight) (Fig. 12) show that the top layer of the upper and lower coils generates strong heat, consistent with the numerical analysis, which showed that the current density concentrates on the top layer of the upper and lower coils. In this coil, because the coil conductor is divided, diffusion of heat by thermal conduction is weak. The heat at the top layer is not transmitted to other layers; therefore, there is only a local temperature rise at the top layer.

The experimental results for the parallel coil (cross) (Fig. 13) show almost uniform current flow in each layer, which is consistent with the numerical analysis. Considering localized heat generation for the straight connection, the main cause of this uniform temperature rise seems to be the uniform current density, not the fast thermal diffusion in the coil.

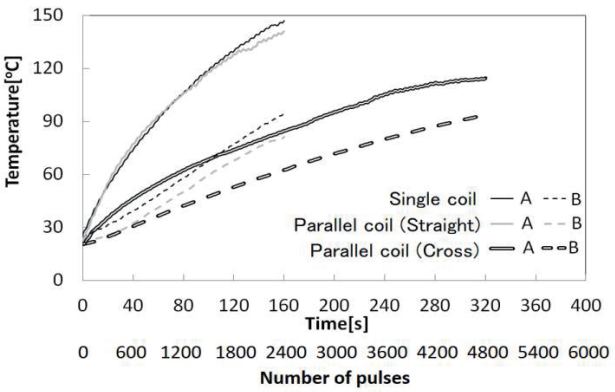

Fig. 14 Temperature increase on coil surface measured by thermocouples.

The temperatures at the coil tip side after 1200 pulses for the single coil, parallel coil (straight), and parallel coil (cross) were 110.4 °C, 112.3 °C, and 67.6 °C, respectively, corresponding to temperature rises from room temperature (22 °C) of 88.4 °C, 90.3 °C, and 45.6 °C, respectively. These results roughly agree with the numerical analysis results shown in Table 1. Considering the amount of heat generation, the temperature rise should be lower in the parallel coil (straight). The reason of unexpected increment of temperature rise in the parallel coil (straight) is the heat in the top layer does not diffuse throughout the coil.

3.2.2 Results of test with thermocouples

Figure 14 shows the results of measuring the time course of the surface temperature of each coil type with thermocouples. This figure shows also the number of generated pulses. The measurements were carried out three times for each coil type. Table 2 shows the means and standard deviations of the number of pulses required for the surface temperature to increase from 30 °C to 80 °C measured at each measurement point three times.

Table 2 Number of pulses required for coil surface temperature to increase from 30 °C to 80 °C.

Coil model	Position	Average ± SD
Single coil	A	635 ± 31
	B	1635 ± 32
Parallel (Straight)	A	575 ± 9
	B	2000 ± 160
Parallel (Cross)	A	1830 ± 150
	B	2995 ± 262

As shown in Fig. 14, for the single coil and the parallel coil (straight), the temperature on the tip side of the coil (A) sharply rises, and that on the base side of the coil (B) also rises but with a delay. There is a large difference between the temperatures at points A and B, indicating that the rise in temperature is biased toward the tip of the coil. Even with the results in Table 2, for the single coil and the parallel coil (straight), the required number of pulses at points A and B are greatly different. The inverse of the required number of pulses corresponds roughly to the amount of heat generated at a point. The difference of required number of pulses thus indicates that heat generation in these coils is strongly biased.

The results for the parallel coil (cross) in Fig. 14 show that although the temperature rise at point A is faster, the difference between temperatures at points A and B is always smaller compared with that for the other two coil types. That is, heat generation bias on the surface of the coil is weaker than other two coil types.

Because the part in contact with the patient is on the tip side of the coil, for practical coils, the temperature rise in this part must be small. As shown in Table 2, at point A, the pulses required for the temperature to increase from 30 °C to 80 °C for the single coil and the parallel coil (straight) are about 600 pulses; that for the parallel coil (cross) is more than 3 times this value. In other words, the latter coil can generate more than 3 times the number of pulses compared with those of the former two coils.

4. Conclusion

The heat generation in a U-shaped core coil during magnetic stimulation was investigated using numerical analysis and experiments. The numerical analysis results reveal that the main cause of the heat generation is the eddy current generated inside the coil conductor by the magnetic flux generated from the core tip. Moreover, an ideal current density distribution can be obtained by dividing the conductor and using an appropriate connection between the divided conductors so that the electromotive forces induced in the conductors cancel each other.

Prototypes of the coil models were manufactured and tested. The experimental results were consistent with the numerical analysis, confirming that heat generation can be greatly suppressed by dividing the conductor and using a proper connection between the divided conductors.

A clinical trial on a dysphagia patient with a stimulation coil based on the proposed technology is currently underway at Fujita Health University. Considering the actual use at the rehabilitation clinic, it is desirable to generate 6,000 pulses in 15 minutes, so further improvement of the stimulation coil is required. In this study, the conductor was divided into five sections and evaluated. However, it may be possible to reduce the bias of the current density further and make a coil with lower heat generation by using finely divided parallel winding coils. However, if the division is excessive, the conductor space factor and the heat dissipation efficiency may decrease. The optimal winding parameters should thus be determined using numerical analysis.

Acknowledgements We thank Adam Przywecki, B.Eng, from Edanz Group (www.edanzediting.com/ac) for editing the English text of a draft of this manuscript.

References

1) P. K. Lieu, M. S. Chong, and R. Seshadri: *Ann. Acad. Med. Singapore*, **30**, 148 (2001).
2) G. C. Remesso, and M. M. Fukujima: *Arq. Neuropsiquiatr*, **69**, 785 (2011).
3) Y. Michiwaki, and Y. Sumi: *Rounenshigaku (in Japanese)*, **28(4)**, 366 (2014).
4) M. Bülow, R. Speyer, L. Baijens, V. Woisard, and O. Ekberg: *Dysphagia*, **23**, 302 (2008).
5) J. W. Park, Y. Kim, J. C. Oh, and H. J. Lee: *Dysphagia*, **27**, 521 (2012).
6) G. D. Carnaby, and L. Harenberg: *Dysphagia*, **28**, 567 (2013).
7) H. Kagaya, M. Baba, E. Saitoh, S. Okada, M. Yokoyama, and Y. Muraoka: *Neuromodulation*, **14**, 278 (2011).
8) S. J. Kim, and T. R. Han: *Neuromodulation*, **12**, 134 (2009).
9) R. Momosaki, M. Abo, S. Watanabe, W. Kakuda, N. Yamada, and K. Mochio: *Neuromodulation*, **17**, 637 (2014).
10) R. Momosaki, W. Kakuda, N. Yamada, and M. Abo: *Int. J. Rehabil. Res.*, **39(3)**, 263 (2016).
11) J. Szecsi, M. Schiller, A. Straube, and D. Gerling: *Arch. Phys. Med. Rehabil.*, **90(4)**, 564 (2009).
12) H. Mori, K. Yashima, H. Kosukegawa, S. Izumi, and T. Takagi: *Baiomekanizumu (in Japanese)*, **24**, 79 (2018).
13) S. Ueno, T. Matsuda, and O. Hiwaki: *J. Appl. Phys.*, **67(9)**, 5838 (1990).
14) H. Kagaya, M. Ogawa, S. Mori, Y. Aoyagi, S. Shibata, Y. Inamoto, H. Mori, and E. Saitoh: *Neuromodulation*, Epub ahead of print.
15) T. Kato, M. Sekino, T. Matsuzaki, A. Nishikawa, Y. Saitoh, and H. Ohsaki: *Seitaiikougaku (in Japanese)*, **50(1)**, 180 (2012).
16) M. Jaritz, and J. Biela: Analytical model for the thermal resistance of windings consisting of solid or litz wire, p1-10 (2013 15th European Conference on Power Electronics and Applications, Lille, 2013).
17) S. Izumi, T. Takagi, R. Nagatomi, N. Nakazato, Y. Yashima, T. Abe: *Rinshoshinkeiseirigaku (in Japanese)*, **37(1)**, 1 (2009).

Received Feb. 22, 2019; Accepted Apr. 09, 2019

Journal of the Magnetics Society of Japan

Vol. 43 No. 4 (通巻第 304号) 2019年 7 月 1 日発行

Vol. 43 No. 4 Published Jul. 1, 2019
by the Magnetics Society of Japan
Tokyo YWCA building Rm207, 1–8–11 Kanda surugadai, Chiyoda-ku, Tokyo 101–0062
Tel. +81–3–5281–0106 Fax. +81–3–5281–0107

Printed by JP Corporation Co., Ltd.
Sports Plaza building 401, 2–4–3, Shinkamata Ota-ku, Tokyo 144–0054
Advertising agency: Kagaku Gijutsu-sha

発行：（公社）日本磁気学会 101–0062 東京都千代田区神田駿河台 1–8–11 東京YWCA会館 207 号室
製作：ジェイピーシー 144–0054 東京都大田区新蒲田 2–4–3 スポーツプラザビル401 Tel.（03）6715–7915
広告取扱い：科学技術社 111–0052 東京都台東区柳橋 2–10–8 武田ビル 4F Tel.（03）5809–1132